STUDY OF ELECTRONIC PROPERTIES OF RHOMBOHEDRAL GRAPHITE USING SCANNING TUNNELING MICROSCOPE

A thesis submitted for the degree of

Master of Science

to the Faculty of Science,

Eötvös Loránd University, Budapest

By

Mohammad Syahid Bin Mohd Isa

Thesis advisor 1: Dr. Peter Nemes-Incze,
Topography in Nanomaterials Lendület Group, Centre for Energy Research

Thesis Advisor 2: Prof. Jenő Kürti
Department of Biological Physics, ELTE

May 2020

Statement of Originality

Name: MOHAMMAD SYAHID BIN MOHD ISA

Neptun ID: VJ3JXB

ELTE Faculty of Science: MATERIAL SCIENCE

MSc specialization: —

Title of diploma work: STUDY OF ELECTRONIC PROPERTIES OF RHOMBOHEDRAL GRAPHITE USING SCANNING TUNNELING MICROSCOPE

As the author of the diploma work, I declare with disciplinary responsibility that my thesis is my own intellectual product and the result of my own work. Furthermore, I declare that I have consistently applied the standard rules of references and citations.

I acknowledge that the following cases are considered plagiarism:

– using a literal quotation without quotation mark and adding citation

– referencing content without citing the source

– representing another person's published thoughts as my own thoughts.

Furthermore, I declare that the printed and electronical versions of the submitted diploma work are textually and contextually identical.

Budapest, 20, MAY 27th

Signature of Student

Preface

Superconductivity in graphene is an elusive phenomenon. It has been shown to exist in alkali intercalation compounds of graphite and more recently in bilayers of graphene twisted by a small angle. In the latter case, the superconducting state is believed to be originated from the flat band in the electronic band structure of the material.

In the flat band region, many body interactions dominate the system, suppressing kinetic energy down to zero. Apart from twisted bilayer graphene, flat band electronic structure was also observed in rhombohedral or also known as ABC graphite. In this configuration, the conduction and valence band have diverged effective mass charge carriers at *K* point unlike massless particles in monolayer graphene. Due to high number of intersection points, large density of states at Fermi level can be observed. On top of that, ABC stacked graphene is surface state system since vertical coupling of atomic sublattices leaves top and bottom atoms with free electrons in p_z orbitals. This makes ABC graphene to be attractive to be investigated with scanning tunneling microscope which is surface sensitive instrument, with the ultimate goal of identifying the nature of the Fermi surface instability in ABC graphite.

In this thesis, experimental work using scanning tunneling microscope on bulk graphite with ABC stacking order is presented. My interest on ABC graphite investigation arises due to no literature published attesting flat band presence in such system to the best of my knowledge. I reveal flat band in ABC stacked region by measuring the sample containing 21 layers forming both ABA and ABC stacking order. I plot the measurements with colormap to demonstrate domain interface of the sample. The extent of flat band can be extracted by the size of the peak in density of states plot which in my case, the bandwidth was found to be 140 meV. From this number, we could compare with other literature about how much number of graphene layer influences the flat band size.

I start this thesis by introducing graphene in general and discuss its electronic band structure and density of states in *Chapter 1*. This followed by other configurations of graphene such as bilayer, trilayer and twisted bilayer graphene. In *Chapter 2*, I present experimental methods

and characterization technique to investigate the material. The results of the investigation are analyzed and discussed in *Chapter 3*. Finally, I conclude my findings and give recommendations for future work in *Chapter 4*.

Contents

Chapter 1

Introduction

Solid state physics has played a central role in the design of the modern electronic device. Conductor, semiconductor and insulator for example, are determined by the band structure of the material. The crystal and atomic configurations of the material define the electronic band structure intrinsically. This classical structure however was broken by the newly found graphene in 2004.

Graphene is a two-dimensional material which has a very different electronic properties from the bulk crystal (graphite). Even though the study on two-dimensional material had begun for decades, the exploration in this field was restricted due to the impossibility to prepare two-dimensional material in the real world especially following arguments of famous physicist Landau and Peierls who suggested no two-dimensional material could exist because of thermodynamic instabilities [1]. The theory suggests that atoms could be displaced at low dimensional crystal lattices as the thickness comparable to the interatomic distance. Mermin further supported this theory with many observable effects in his experimental works [2]. Though the existence is yet to be proven, the idea of having two-dimensional material has been agreed as an “academic material” to describe various phenomena such as fullerene and nanotube [3]. In 2004, Andre Geim and Nosolevov had successfully isolated one to few layers of carbon atoms from graphite, and after many experiments, confirmed the existence of two-dimensional material in the form of graphene. Graphene was found to host relativistic Dirac charge carriers which was never found in any material before [4].

The electronic properties of graphite are determined by the p_z orbitals of carbon, with charge carrier hopping in the honeycomb planes of the graphene layers and intralayer hopping between layers [5]. The lack of intralayer hopping, along with the honeycomb lattice of graphene is responsible for the appearance of Dirac quasiparticles as charge carriers. If two layers of graphene are stacked on top of each other, interlayer hopping dominates the system.

This can be observed in AB or also known as Bernal configuration where massive Dirac quasiparticles act as charge carriers with the possibility of opening a band gap in a transverse electric field [6]. This bilayer graphene if stacked at some twisting angle with mismatch of the order 0.5 - 1^{o} could result a flat band near the Dirac point and the material becomes a superconductor at partial filling of the flat band [7]. Third graphene layer if added on top of AB configuration gives two possibilities for stacking: ABA and ABC, as explained in the next chapters. ABC stacking, also called rhombohedral graphite, again due to the different interlayer hopping pattern has a very different electronic structure to Bernal stacked (ABA) graphite. In ABC configuration, the bulk is gapped with the top and bottom graphene layers hosting a flat surface state that is prone to Fermi surface instabilities [8], with a bandwidth that decreases with the number of layers, *N* [9]. Thus, ABC graphite presents a new platform to study many body instabilities in a flat electronic band, without the need to stack graphene layers at a precise angle, as in twisted bilayer graphene.

Thick layers of ABC graphite ($N > 10$ layers) have been investigated by angle resolved photoemission (ARPES) and charge transport measurements, but the surface state has not been studied on the atomic scale by scanning tunneling microscopy (STM). In my thesis I present the first steps towards investigating thick ABC graphite crystals by STM, including sample preparation, contacting of the graphite flakes and first STM investigations at room temperature.

1.1 Graphene: An Overview

In nature, carbon is the key ingredient that forms many important molecules in both living and non-living things. Being the sixth most abundant element in the universe, carbon appears in various morphologies including in mineral form of diamond and graphite which comprises carbon atoms arranged in different ways. Graphite is made of a linked hexagonal network of carbon atom forming layers, connected with Van der Waals bonds between adjacent layers. The isolation of one layer of graphite with very high crystallinity and purity is called graphene. This can be achieved by mechanical exfoliation and was proven to be feasible by Andre Geim and Nosolevov in 2004. Their experiment revealed remarkably unique properties of graphene

where charge carriers behave as Dirac fermions [4]. This discovery awarded them with Nobel Prize in 2010.

Since the discovery, more synthesis methods have been tried and reported in the literature such as unzipping carbon nanotube [10], chemical exfoliation of graphite [11], CVD technique [12] and thermal decomposition of SiC [13]. CVD for example has entered the mass production stage but still faces some challenges especially to produce high quality graphene to be used in electronic devices.

Graphene possesses extremely high charge carrier mobility exceeding 15 000 $cm^2 V^{-1} s^{-1}$ even at room temperature due to zero-overlap of conduction and valence band which make them semimetal by nature [3]. Electrons near the Dirac point have zero effective mass. By manipulating the stacking to form bilayer, trilayer or twisted bilayer graphene, electronic properties change distinctively which suggest possibilities to be used as a superconductor [7][14] and topographical insulator [15]. Besides that, graphene also known for being the material with highest strength to weight ratio. This could be understood by the single sheet of carbon atoms which hold each other with strong σ-bond. The Young's modulus of graphene was recorded on the order of 1 TPa and its intrinsic strength around 130 GPa [16].

Graphene is made up of honeycomb lattice with each unit cell made from two carbon atoms with non-equivalent sublattices labeled as *A* and *B* as shown in Figure 1. These atoms are connected by σ bonding through hybridization of three atomic orbitals *s*, p_x, and p_y forming strong sp^2 bonds. At the top and bottom of the layer, p_z orbitals with one electron each are unpaired allowing for π-bond to contact another atom from the neighboring layer. The energy in σ-bond is huge as the electronic bands are filled completely compared to π bands. This is the reason why graphene possesses high mechanical strength. The interatomic distance of adjacent C-C atom is δ = 0.142 nm, lattice constant a = 0.246 nm and thickness of a layer is approximately d = 0.335 nm.

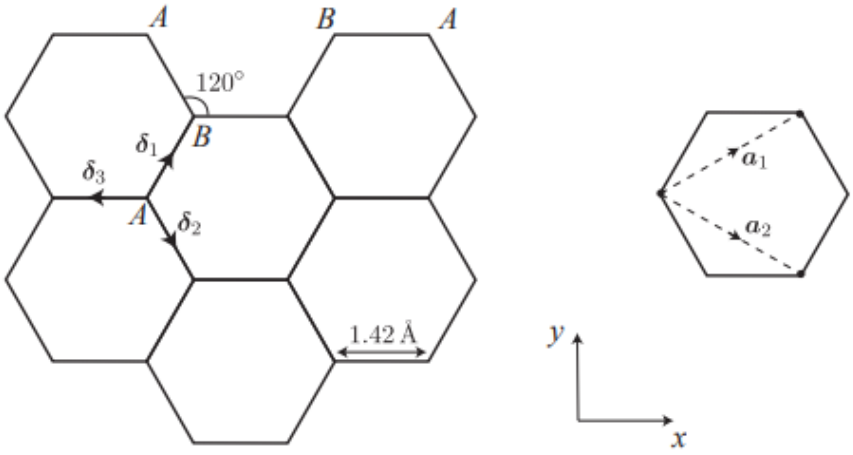

Figure 1: Unit cell of graphene made up from two non-equivalent atom, A and B. Primitive lattice vector is described by $\mathbf{a}_n$ *and nearest neighbor vector by* $\boldsymbol{\delta}_n$*. Image reproduced from ref [17].*

The Bravais lattice for graphene has primitive lattice vectors $\mathbf{a}_1$ and $\mathbf{a}_2$ described as:

$$\mathbf{a}_1 = \frac{a}{2}(3, \sqrt{3}), \qquad \mathbf{a}_2 = \frac{a}{2}(3, -\sqrt{3})$$

The reciprocal lattice vectors in the Brillouin Zone (BZ) are spanned by:

$$\mathbf{b}_1 = \frac{2\pi}{3a}(1, \sqrt{3}), \qquad \mathbf{b}_2 = \frac{2\pi}{3a}(1, -\sqrt{3})$$

The Brillouin Zone (BZ) of graphene is a hexagon as shown in Figure 2. With two inequivalent sublattices, all six points in each corner can be grouped as two non-equivalent corners which are labeled as *K* and *K'*.

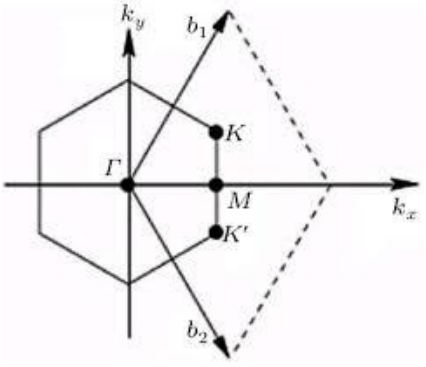

Figure 2: Brillouin Zone of graphene is hexagonal with two different edges labelled as K and K'. The reciprocal lattice vector is represented by $\mathbf{b}_n$*. Image ref [18].*

1.2 Monolayer Graphene (MLG)

The calculations to describe electronic band structure of graphene using tight-binding approximation as described by McCann are briefly presented here [5]. We start with Schrödinger equation which defines the behavior of electrons behavior in the crystal.

$$\hat{\mathrm{H}}|\boldsymbol{\Psi}\rangle = \boldsymbol{E}|\boldsymbol{\Psi}\rangle$$

where $\hat{\mathrm{H}}$ is the Hamiltonian operator, $|\boldsymbol{\Psi}\rangle$ is wavefunction and $\boldsymbol{E}$ is total energy of the electron in the system. By only considering nearest-neighbor interaction, the Hamiltonian reads:

$$\hat{\mathrm{H}} = -\mathbf{t}\sum_{\langle \mathrm{ij}\rangle}(\mathbf{a}_\mathrm{i}{}^\dagger\mathbf{b}_\mathrm{j} + \mathbf{b}_\mathrm{j}{}^\dagger\mathbf{a}_\mathrm{i})$$

where $\mathbf{t}$ is nearest neighbor intralayer hopping energy, $\mathbf{a_i}^\dagger$ is fermionic operator that creates electron in the *A* sublattice and $\mathbf{a_i}$ the one that do the electron annihilation. Similarly for $\mathbf{b_i}^\dagger$ and $\mathbf{b_i}$ for the *B* site. We then use:

$$\mathbf{a}_\mathbf{i}{}^\dagger = \frac{1}{\sqrt{N/2}}\sum_{\mathbf{k}} e^{i\mathbf{k}.\mathbf{r_i}}\ \boldsymbol{a}_\mathbf{k}{}^\dagger$$

where *N/2* is the number of sites for *A* sublattice and similarly for *B* sublattice using $\mathbf{b_i}^\dagger$. We take $\boldsymbol{\delta}$ as sum of nearest-neighbor vector of $\boldsymbol{\delta}_1$, $\boldsymbol{\delta}_2$ and $\boldsymbol{\delta}_3$ as shown in Figure 1. The sum over nearest neighbor then can be rewritten as:

$$\sum_{\langle \mathrm{ij}\rangle}(\mathbf{a}_\mathrm{i}{}^\dagger\mathbf{b}_\mathrm{j} + \mathbf{b}_\mathrm{j}{}^\dagger\mathbf{a}_\mathrm{i}) = \sum_{\mathrm{i}\in A}\sum_{\boldsymbol{\delta}}(\mathbf{a}_\mathrm{i}{}^\dagger\mathbf{b}_{\mathrm{i}+\boldsymbol{\delta}} + \mathbf{b}_{\mathrm{i}+\boldsymbol{\delta}}{}^\dagger\mathbf{a}_\mathrm{i})$$

Combining all these, we get Hamiltonian for graphene as:

$$\hat{\mathrm{H}} = -\frac{\mathbf{t}}{N/2}\sum_{i\in A}\sum_{\boldsymbol{\delta},\mathbf{k},\mathbf{k}'}(e^{i\left(\mathbf{k}-\mathbf{k}'\right).\mathbf{r}_i}\ e^{i\mathbf{k}'.\boldsymbol{\delta}}\ \boldsymbol{a}_\mathbf{k}{}^\dagger\ \boldsymbol{b}_{\mathbf{k}'} + \mathbf{H}.\mathbf{c})$$

We substitute

$$\sum_{i\in A} e^{i(\mathbf{k}-\mathbf{k}')}.\mathbf{r_i} = \frac{N}{2}\boldsymbol{\delta}_{\mathbf{k}\mathbf{k}'}$$

Then, our Hamiltonian become:

$$\hat{\mathrm{H}} = -\mathbf{t}\sum_{\delta,\mathbf{k}} \left(e^{-i\mathbf{k}.\boldsymbol{\delta}}\, \mathbf{a_k}^{\dagger}\, \mathbf{b_k} + \mathbf{H.c}\right)$$

$$= -\mathbf{t}\sum_{\delta,\mathbf{k}} \left(e^{-i\mathbf{k}.\boldsymbol{\delta}}\, \mathbf{a_k}^{\dagger}\, \mathbf{b_k} + \mathbf{e}^{\mathbf{ik}.\boldsymbol{\delta}}\, \mathbf{b_k}^{\dagger}\, \mathbf{a_k}\right)$$

We can express Hamiltonian to a more general form as:

$$\hat{\mathrm{H}} = \sum_{\mathbf{k}} \boldsymbol{\psi}^{\dagger}\, \mathbf{h}(\mathbf{k})\; \boldsymbol{\psi}$$

where

$$\boldsymbol{\psi} = \begin{pmatrix}\mathbf{a_k}\\ \mathbf{b_k}\end{pmatrix}, \qquad \boldsymbol{\psi}^{\dagger} = \begin{pmatrix}\mathbf{a_k}^{\dagger} & \mathbf{b_k}^{\dagger}\end{pmatrix}, \qquad \mathbf{h}(\mathbf{k}) = -\mathbf{t}\begin{pmatrix}0 & \Delta_{\mathbf{k}}\\ \Delta_{\mathbf{k}}^{*} & 0\end{pmatrix} \quad \text{and} \quad \Delta_{\mathbf{k}} = \sum_{\boldsymbol{\delta}} e^{i\mathbf{k}.\boldsymbol{\delta}}$$

with **h**(**k**) is the matrix representation for monolayer graphene. $\Delta_{\mathbf{k}}$ can be calculated for each term of **δ** as:

$$\Delta_{\mathbf{k}} = e^{i\mathbf{k}.\delta_1} + e^{i\mathbf{k}.\delta_2} + e^{i\mathbf{k}.\delta_3}$$

$$= e^{i\mathbf{k_x}.\mathbf{a}}\left[1 + 2e^{i3\mathrm{k_x a}/2}\cos\left(\frac{\sqrt{3}}{2}k_y a\right)\right]$$

With eigenvalue $\mathbf{E}_{\pm} = \pm\mathbf{t}\sqrt{\Delta_{\mathbf{k}}\Delta_{\mathbf{k}}^{*}}$, we calculate energy band as follow.

$$\mathbf{E}_{\pm}(\mathbf{k}) = \pm\mathbf{t}\sqrt{1 + 4\cos\left(\frac{3}{2}k_x a\right)\cos\left(\frac{\sqrt{3}}{2}k_y a\right) + 4\cos^2\left(\frac{\sqrt{3}}{2}k_y a\right)}$$

This normally simplified as $\mathbf{E}_{\pm} = \pm\mathbf{t}\sqrt{3 + \mathbf{f}(\mathbf{k})}$ where:

$$\mathbf{f}(\mathbf{k}) = 2\cos\left(\sqrt{3}k_y a\right) + 4\cos\left(\frac{3}{2}k_x a\right)\cos\left(\frac{\sqrt{3}}{2}k_y a\right)$$

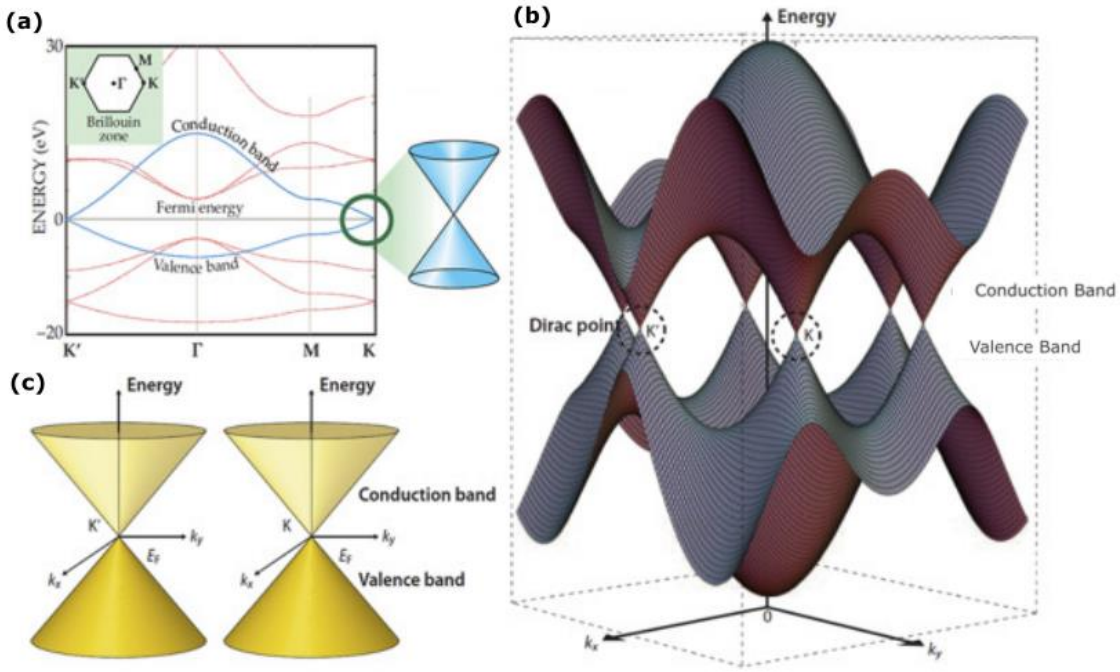

Figure 3: (a) Energy band structure of graphene showing linear dispersion near K point, (b) image showing all Dirac point in the six edges of Brillouin Zone and (c) Dirac cone showing intersection of conduction band and valence band. Image reproduced from ref [19]

The calculation of the energy band within the tight binding approximation shows the linear band crossing near the *K* point. In k_x and k_y space, we obtain conical shape of the band structure which famously known as Dirac cone. The total number of intersections are six at the edge of Brillouin Zone. Electrons near the Fermi level can be considered as massless Dirac fermions which means the particles have zero rest mass and travel with the Fermi velocity, which is analogous to the speed of light.

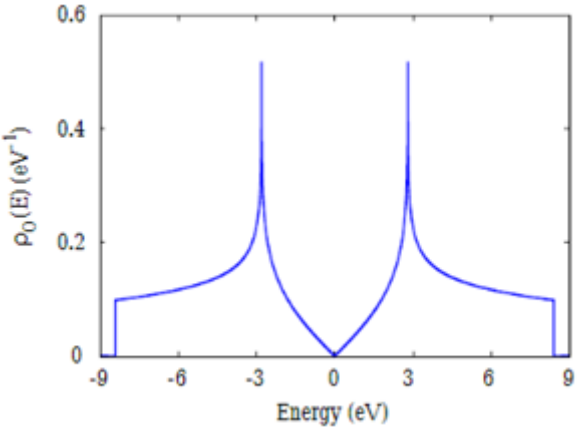

Figure 4: Density of states of monolayer graphene is linear close to Fermi level and vanishes as it approaches zero. Image reproduce from ref [20].

The density of states (DOS) of single layer graphene is shown in Figure 4 with the DOS going to zero at Fermi level. This indicates the semi-metallic properties of graphene where conduction and valence band overlap at a point. The description for this curve is true for undoped and perfectly layered graphene with no defects on the sheet.

1.3 Bilayer Graphene (BLG)

In the case of two-layers of graphene, we can either place the second layer atoms directly on top of first layer atoms (AA) or place one sublattice of the bottom layer on top of the other sublattice in the top layer (AB). While the distance between in-plane carbon atoms is the same for both AA and AB stacking which is 0.142 nm, the separation between layers was found to be different, which is 0.359 nm for AA and 0.331 nm for AB stacking [21]. This can be understood by how the positioning of carbon atoms in the structure affects the van der Waals interactions as shown in Figure 5 below.

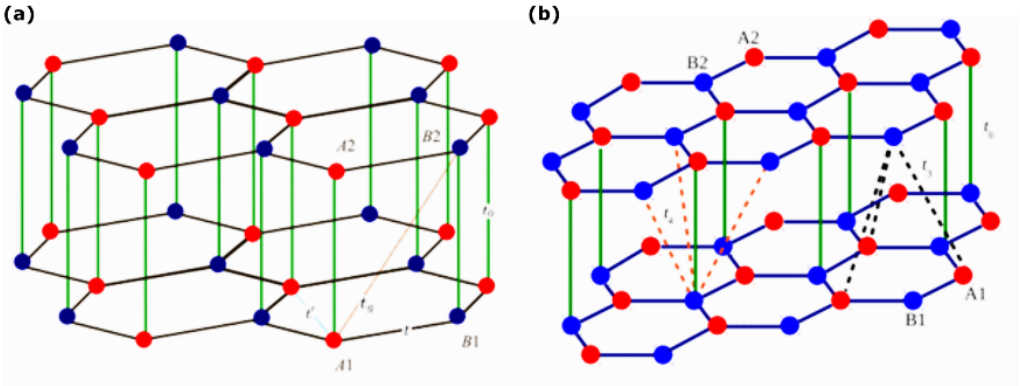

Figure 5: Bilayer graphene with stacking order (a) AA and (b) AB. Image reproduced from ref [22].

This difference in positioning of atoms directly affects its electronic properties as the overlap of the p_z orbitals differs for the two stackings. AB-stacking has the lowest energy and thus is the most stable phase among other stacking orders [23].

To calculate the band structure, I present the results of tight binding calculation done by Tabert et al. [24], which includes interaction with the nearest atoms hopping parameter. The energy dispersion relation of AB stacking when plotted shows parabolic curve which touches Fermi level at the *K* point instead of a Dirac cone like in the case of monolayer graphene (see

Figure 6). Near the Fermi level, the charge carriers in bilayer graphene can be considered as massive Dirac fermions.

AA stacking on the other hand poses linear band structure similar to monolayer graphene, with the difference being that the intersections at the *K* point are found to be shifted in energy. To understand the origin of this comparison, we should look into the unit cell of AA stacked graphene which contains four atoms with two atoms are identical and placed directly vertical to each other as shown in Figure 5a. The energy bands as described by Tabert is given as:

$$\mathbf{E}_n(\mathbf{k}) = \pm[|\mathbf{f}(\mathbf{k})| \pm \gamma_n$$

where *n* is graphene layer in top or bottom position, $|\mathbf{f}(\mathbf{k})|$ is the energy dispersion for monolayer graphene and $\boldsymbol{\Upsilon}$ is nearest neighbor interlayer hopping parameter . From this, we observe the bands structure of monolayer graphene are shifted in energy by -$\boldsymbol{\Upsilon}$ and +$\boldsymbol{\Upsilon}$.

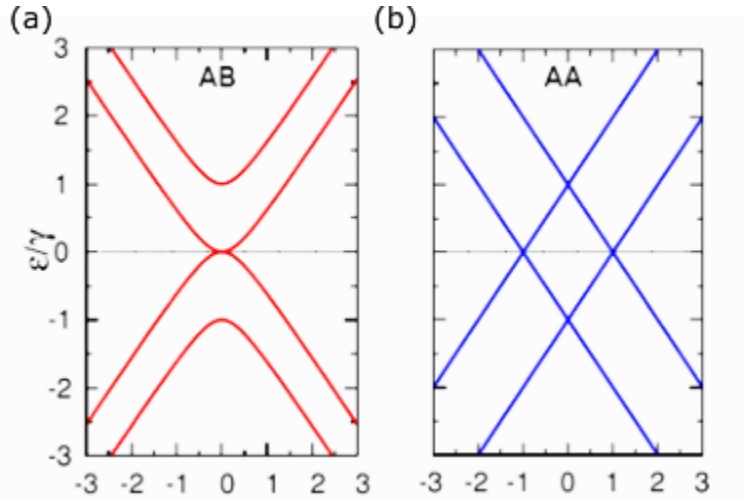

Figure 6: Electronic band structure calculated using tight-binding approximation considering only nearest neighbour parameter of (a) AB stacked graphene showing parabolic curve with conduction and valence band touches at Dirac point, (b) AA-stacked graphene gives linear dispersion with intersection shifted in energy from Fermi level by $\pm\boldsymbol{\gamma}$ *. Image ref [24].*

As for the density of states (DOS) for AB stacking, the calculation of Tabert indicates that near the Fermi level, the DOS is non-zero unlike in monolayer graphene due to the effect of nearest-neighbor hopping parameters from the second layer. This finite DOS is a result of parabolic energy dispersion. This is similar to AA stacking with the exception the function is flat near Fermi level **E** = 0 as shown in Figure 7.

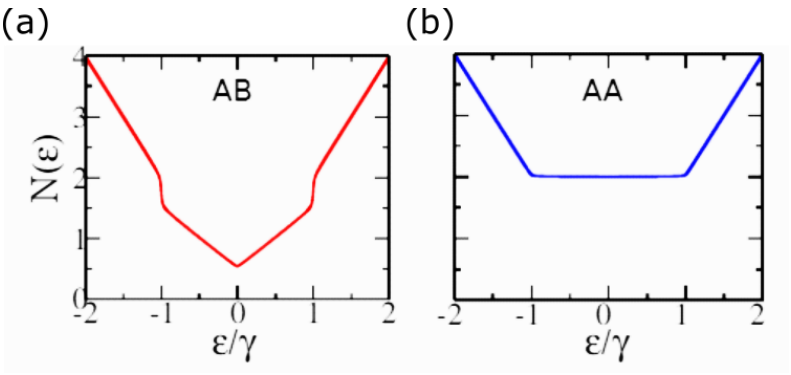

Figure 7: (a) DOS of AB stacked graphene shows non-zero DOS unlike in monolayer graphene band structure. (b) Calculated DOS for AA stacked graphene with flat function near the Fermi energy. Image ref [24].

1.4 Few layer Graphene (FLG)

Let us consider adding more layers to the crystal structure of graphene to understand the influence of the number and stacking arrangement of the layers on the electronic properties. For the third layer, energetically favored stacking configurations are ABA and ABC.

ABA is famously known as Bernal stacking, which is energetically the most stable stacking order. In this configuration, the atoms in the third layer are directly located perpendicular to atoms in the first layer, thus repeating the sequence every two layers. The carbon atoms in the third layer of ABC stacking which also known as rhombohedral stacking on the other hand are positioned at nearest neighbor distance away with respect to the layer labeled A (See Figure 8).

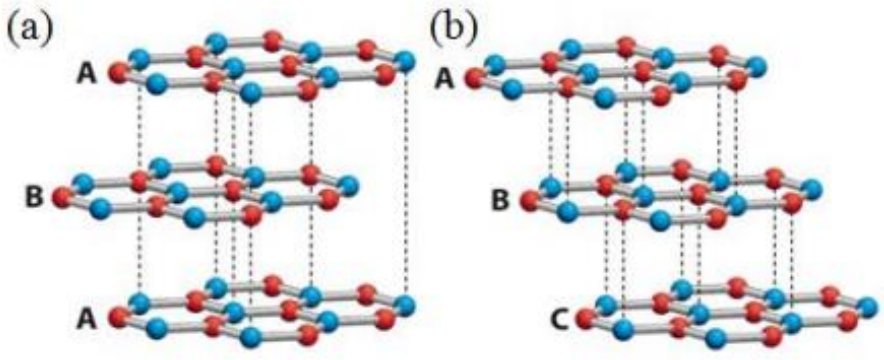

Figure 8: Atomic configuration of (a) ABA and (b) ABC stacked trilayer graphene. Red and blue atom represent two sublattices of graphene unit cell. Dashed line indicates the atomic interlayer interaction. Image ref [8].

Here, I present the result of tight binding calculation of trilayer graphene done by Que et al. [25] to explain the electronic properties of multilayer graphene. In Figure 9, the band structure

of ABA stacking shows linear band in magenta, crossing at the Dirac point at K, similar to the band structure of monolayer graphene. The green parabolic curve representing the conduction and valence bands touch at Dirac point. These intersections result in a v-shaped DOS, having a finite minimum value at the Fermi level. In ABC stacking on the other hand, one pair of conduction and valence bands touch at the *K* point and forming a flat band. This flat band dispersion results in a higher value of the DOS close to Fermi level which can be seen as a peak at zero energy. In both side of DOS vs Energy curve, we can see another pair of small peaks at higher energies. This is the result of intersection of two band in the *K* point but at higher energies above and below the Fermi level.

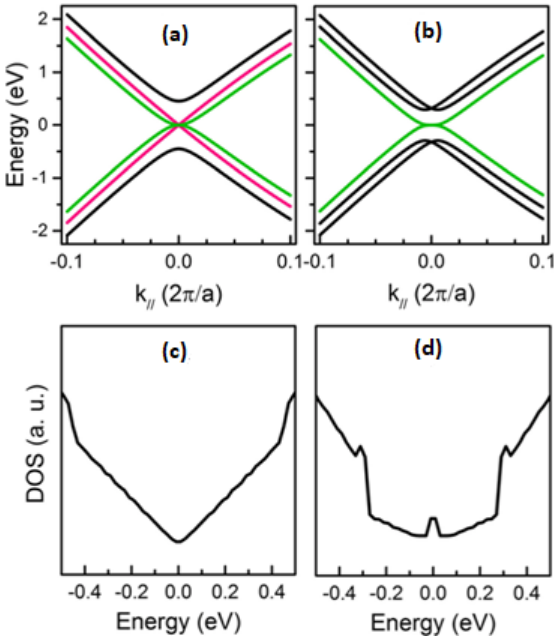

Figure 9: Image showing (a) calculated electronic band structure of ABA and (b) ABC graphene, density of states for (c) ABA and (d) ABC graphene respectively. Image ref[25].

Min and MacDonald [9] have calculated the band structure of ABC stacked graphene as a function of the number of layers using π-continuum model. From the stacking order (see Figure 8b), we may notice the presence of vertical hopping from all red sublattice (α) from top layer and all blue sublattice (β) from bottom layer. By assuming low energy case where interlayer hopping is zero, the α-β pair would form symmetric-antisymmetric doublet (shaded region) with energies $\pm\mathbf{t}_{\perp}$ which then makes the only possible low energy states exists in top and bottom unpaired α and β as shown in Figure 10c. The effective Hamiltonian of ABC stacked N-layer graphene is:

$$\mathbf{H}_N^{eff}(\mathbf{k}) = -\mathbf{t}_{\perp}\begin{pmatrix} 0 & (\boldsymbol{\nu}^{\dagger})^N \\ (\boldsymbol{\nu})^N & 0 \end{pmatrix}$$

where **k** is momentum and **v** is Fermi velocity. The corresponding energy spectrum then:

$$\mathbf{E}^{\pm}_{\mathbf{eff},\mathbf{k}} = \pm \mathbf{t}_{\perp} \left(\frac{\mathbf{v}|\mathbf{k}|}{\mathbf{t}_{\perp}} \right)^{N}$$

We can observe that near the Fermi level, the energy has a power law dependence on the number of layers, *N*. This means that the band gets flatter with wider range of momentum as we increase *N*. Figure 10 shows the difference between (a) trilayer and (b) tetralayer ABC stacked graphene where adding just one more layer signifies observable effect on the overlapping of conduction and valence band.

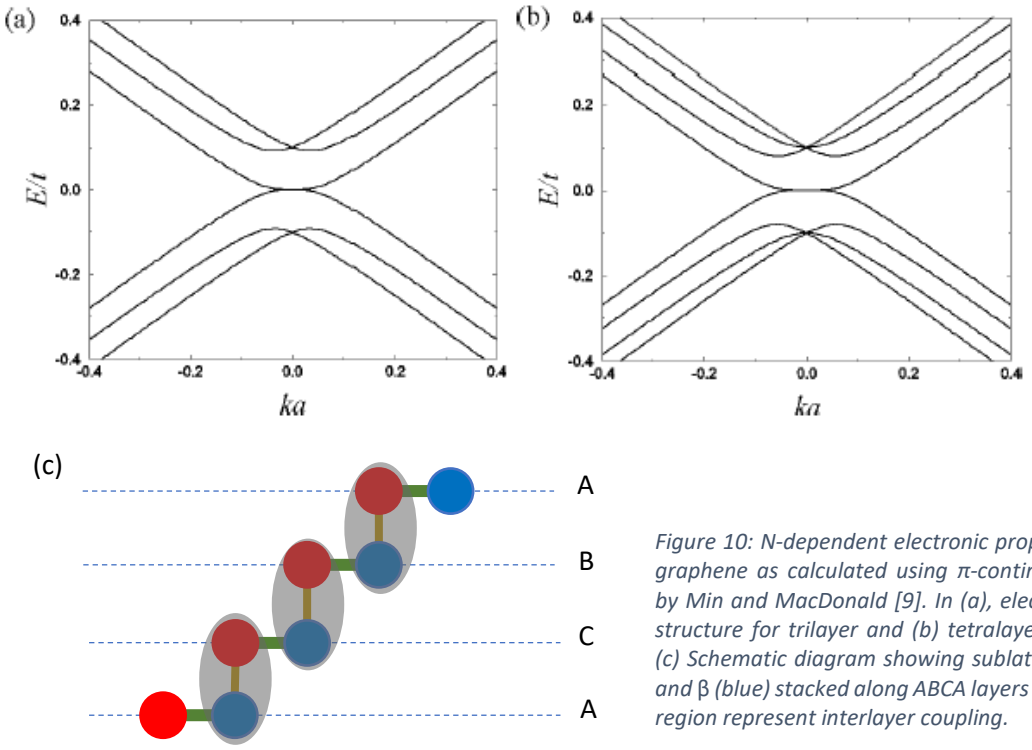

Figure 10: N-dependent electronic property of ABC graphene as calculated using π-continuum model by Min and MacDonald [9]. In (a), electronic band structure for trilayer and (b) tetralayer graphene. (c) Schematic diagram showing sublattices α (red) and β (blue) stacked along ABCA layers with shaded region represent interlayer coupling.

However, other calculation with magnetic instabilities which include spin polarization using first principle as described by Henck et al. [8] shows a gap opening in the flat band region. This was proved with ARPES measurements on ABC graphene where the occupied part of the flat band was found to bend away from Dirac point. The calculation with (see Figure 11a) and without (Figure 11b) spin polarization using the CRYSTAL code proves this effect. The inclusion of spin polarization in the band structure indicates many body interactions exists in ABC graphite system with magnetic instabilities due to surface state of the system as shown in Figure 10c above. The top and bottom layers are predicted to be antiferromagnetically

coupled whereas the spin state in-plane are ferrimagnetic [26]. The antiferromagnetic ground state could be the source of the gap opening in the flat band region.

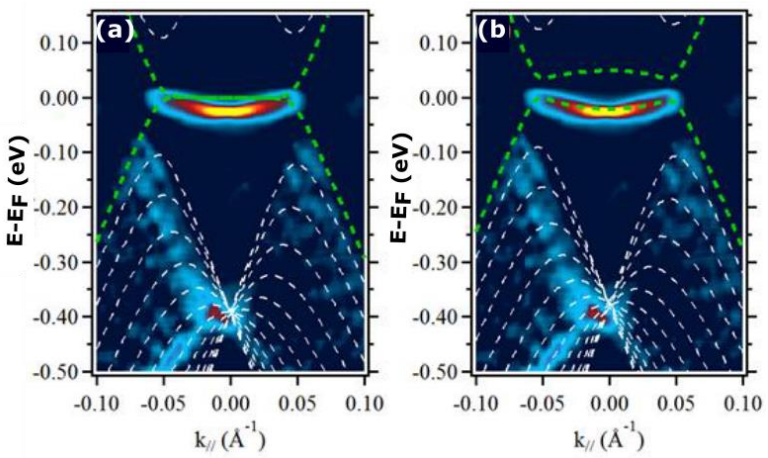

Figure 11: ARPES electron intensity map showing band structure of ABC stacked graphene with N = 14 layers. Image ref [8].

1.5 Twisted Bilayer Graphene (TBG)

Another configuration where the flat bands can be achieved is twisted bilayer graphene (TBG). This interesting attribute was discovered by Pablo Jarillo-Herrero and colleagues from MIT in 2018 with their observation of superconductivity by vertically stacked two sheets of graphene with a mismatch ("magic") angle of 1.16^o [7]. This caught huge attention since the discovery of graphene in 2004 because monolayer graphene is not superconducting on its own.

The hybridization of bands in bilayer graphene change the low energy band structure and by twisting the graphene sheets, a quasiperiodic structure or hexagonal moiré pattern is formed at larger length (15.2 nm) as compared to the graphene lattice constant, a = 0.246 nm [27]. Magic angle which is perfect twisting angle to form flat band near Fermi energy was firstly calculated by Bistritzer and MacDonald exists at θ=1.1^o [28].

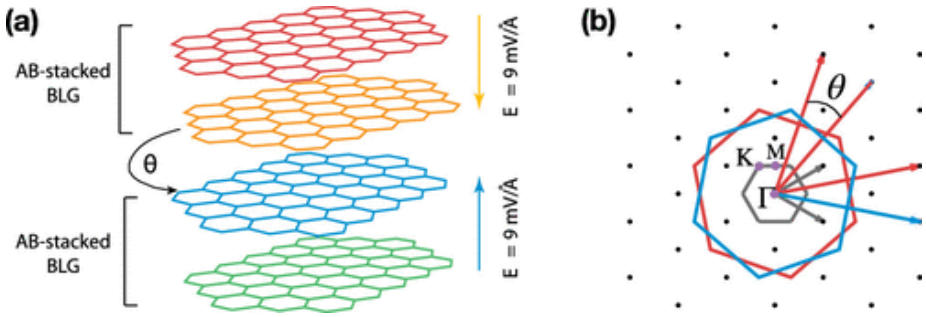

Figure 12: (a) Twisted bilayer graphene can be achieved by arranging two AB stacked bilayer graphene at some twisting angle, θ. (b) Brillouin zone of twisted bilayer graphene is shown in grey whereas for each bilayer is shown in red and blue. Image ref [29].

In the flat band region for different charge densities of the band, an insulating phase which behaves like Mott insulator and superconductor is observed. In the case of the Mott insulator, the material behaves like an insulator even though it is a metal because of strong electron-electron interactions. The superconducting state is detected at temperatures below than 1.7K [7]. Even though the experiment was done at low temperature, the observation of Mott insulator phase next to the superconductor phase suggests that TBG behaves similarly to high temperature superconductors, which are considered to be doped Mott insulators.

Besides that, energy band structure in this region not just flat but was found to be separated between conduction and valence band by single particle gaps with bandwidth in the range of 5 – 10 meV. Haddadi et al. [29] studies the electronic properties of TBG via tight binding approximation (TB) and Density Functional Theory (DFT) calculations with interest to study the evolution of band structure as twist angle changes. Figure 13a and 13b shows the band structure of two different twist angles TBG for both calculation methods. In both cases, we could observe a flat band near the K point with lower angles giving a wider range of dispersion near K point. Another interesting remark in the DFT calculation is the opening of a gap in between conduction and valence band near parabolic curve where they supposed to touch. This was confirmed with TB model with inclusion of intrinsic symmetric polarization which considers the lattice relaxation effects.

In figure 13c, the calculated DOS of TBG with twisting angle θ = 1.05° in light blue line is shown. For comparison, the DOS for two layers of freestanding graphene with no twisting angle and interlayer interaction multiplied by 1000 is plotted together. Energy at Fermi level, E_F is shown in red dashed line calculated based on density $n = -{}^{n_s}/_{2}$ where n_s is superlattice density.

We could observe that the DOS of the flat band configuration gives two peaks about three orders of magnitude higher than two layers. However, the energy required to fill half a band does not coincide with the DOS peaks.

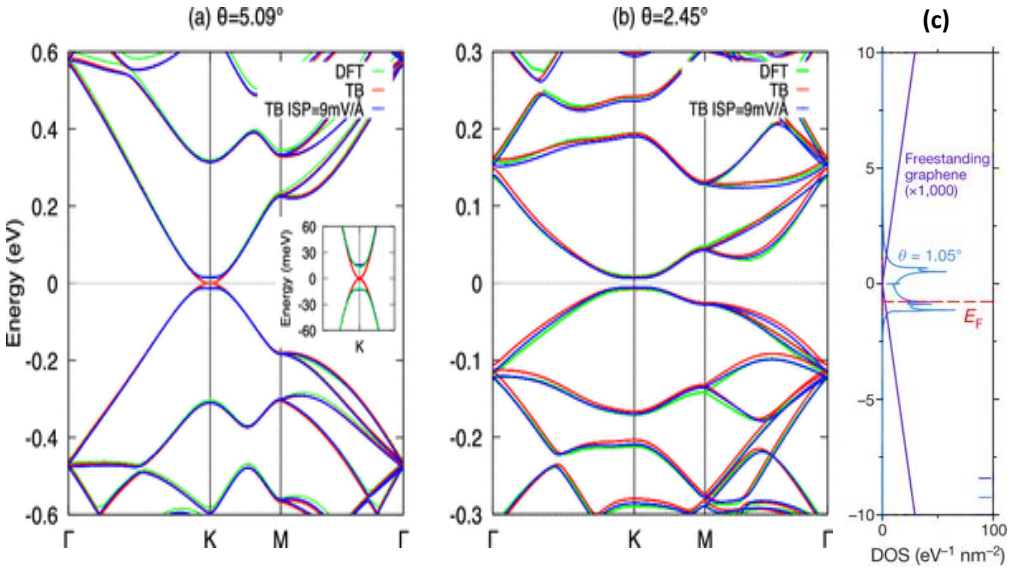

Figure 13: Band structure of TBG with twisting angle (a) θ = 5.09 ° and (b) θ = 2.45 ° calculated using DFT (green), TB approximation (red) and TB with intrinsic polarization considered (blue). In (c), Energy vs DOS is shown for TBG with twisting angle θ = 1.05 ° in light blue and two freestanding graphene stacked at zero twisting angle magnified by 1 000 as shown in purple. Image ref [29].

1.7 Research Motivation

Interest in graphene research has accelerated ever since its discovery in 2004. The research mainly focused on fundamental physics, characterization and real-world application. In the previous subchapter, we discussed that flat bands host many body interactions driven ground states. The reason for this is that the kinetic energy is suppressed with respect to many body effects such as Coulomb interaction between electrons. This is the reason why the flat band regime may potentially be useful in applications such as high temperature superconductors. In addition to that, flat band overlapping between conduction and valence band could be tuned to form bigger gap by application of transverse electric field which may suggest prospective application in semiconductor device [6]. The physics behind this is still under investigations. However, recent developments demonstrate that this can be explained with stabilization of magnetics in the system [26]. The bulk graphite with ABC configuration is gapped with the top and bottom layer left with antiferromagnetic like state since the interlayer has strongly coupled between atoms that located vertically (see figure 10c). With this

coupling, the only magnetic state presence is in-plane weak ferromagnetic. This causes magnetic instabilities, which if stabilized by spin polarization can be the source of band gap opening.

I have shown above that for graphene, the source of flat bands may come from two configurations: ABC stacking and twisted bilayer graphene (TBG). Both cases pose different challenges regarding the design of the devices and applications. In TBG, most of the challenge lies in the fabrication of the phase where bringing the top layer to an intended angle could not easily be done in mass production. The fabrication technique is still researched heavily with some laboratories using the so-called ”tear-and-stack technique” [30]. On the other hand, ABC stacking of graphite could be found at smaller percentage than ABA in nature and in exfoliated graphite flakes. This is because the ABC stacked configuration is known to be less thermodynamically metastable. While the stacking may change from ABC to ABA at temperature higher than 1000^{o}C, it was reported that molecular adsorption may reduce the thermal barrier of reconfiguration down to 150^{o}C [23]. Another interesting way to change the stacking order is via shear stress applied across the layers as discussed by Nery et al [31] and by using charge carrier doping which effectively modifies the energy difference between different stackings [32].

Even with all these challenges, the potential that flat band dispersion promises is huge. As for us, the investigation should also tackle the most abundant and stable form which is bulk graphite. Bulk graphite represented as graphene with at least ten layers is much easier to fabricate under controlled conditions. To our knowledge, there has been no investigation of the density of states for ABC stacked bulk graphite using Scanning Tunneling Microscopy (STM) even though STM is a surface sensitive technique and ABC graphite is surface state system.

To begin, we should confirm the presence of ABC stacking in the graphite. To do this, I prepare the sample containing both ABA and ABC stacking. The different stacking regions are identified by Raman spectroscopy. Then, I have used STM/STS technique to measure the density of states of the samples.

Chapter 2

Experimental and Characterization Technique

In this chapter, the procedures that have been used to conduct the experiments and characterization techniques adopted to analyze the data are described. The chapter starts with the method to prepare the graphite sample on a substrate using mechanical exfoliation. Next, metal contacts preparation technique is discussed for which the contacts were used to connect electrically the sample to the STM holder using two methods; Field's metal based micro-soldering and thermal evaporation of gold with a TEM grid acting as a stencil. Then, optical microscopy is used for imaging of the sample. Similarly imaging at higher magnification could be done using AFM by measuring the topography of the sample surface. Raman spectroscopy was used to locate the ABC and ABA sections of the sample. Finally, measurement using STM to study the electronic properties of the rhombohedral section is described. The brief description on data processing method using Python is presented at the end of the chapter. The exfoliation and initial Raman identification of ABC flakes was done by Krisztián Márity during his summer internship with our group, while my work involved testing the various electrical contacting techniques, AFM investigation, subsequent Raman measurements and STM measurements.

2.1 Material Preparation

2.1.1 Mechanical Exfoliation of Graphite Flake

In the first discovery of graphene, two scientists from the University of Manchester, Andre Geim and Konstantin Novoselov realized the possibility to isolate a layer of graphene from graphite [4]. This technique which also known as the "scotch tape" method exploits the weak bonds between atomic planes of graphite. The van der Waals interactions between planes can simply be countered with normal loads from the release of scotch tape while maintaining the two-dimensional structure due to strong sigma bond between carbon atoms. By repeatedly peeling the layers of graphite, it is possible to reach one layer of graphene.

In our experiments however, the peeling of layers with scotch tape were made only few times since our main interest is to study the thick graphite. The samples were prepared from natural graphite (graphenium) purchased from NGS Naturgraphit GMBH. After few times of peeling by the adhesive tape, we place the remaining layers onto Silicon Oxide SiO_2 wafer that act as a substrate.

It is possible to observe the deposited layers of graphite under an optical microscope. This might be the most important part of the material preparation, which is to identify the best sample to be used in the experiment. Figure 14 shows some of graphite flakes on the substrate. Here we could differentiate between one to few layers of graphene to thick graphite by observing the color of the flake. Liew et al. [33] characterized the optical absorbance of graphene at only 2.3% which means it is almost invisible with naked eyes on surface of substrate. The more layers of graphene there are on the substrate, the more visible it is. Thick sample could easily be identified with a solid and shiny color.

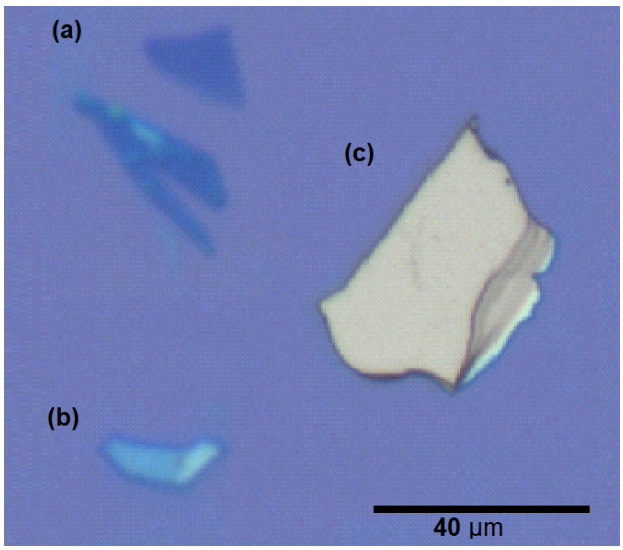

Figure 14: Different form of graphite flakes after peeled using scotch tape. (A) is graphene with number of layers N < 5, (B) N < 20 and (C) is thick graphite containing N > 100 layers.

Other criteria to be considered is the size of the sample. Large size is preferred to make metal contacts with at least 15x15 μm^2 of area remaining for STM measurements.

2.1.2 Metal Contact to Sample

In order to be used STM, the sample need to be electrically connected to sample holder. I present in this thesis two methods which have been used and some of the challenges and benefits for each.

Using Field's Metal Contact

My first tested method consists of soldering to graphite flakes, using a very sharp metal spike. The method is inspired by the technique developed in the Zettl group, using indium [34]. In this method, Field's metal which is a eutectic alloy of Bi, Sn and In was used. To effectively achieve this, I prepared long and sharp spikes by pulling needles from a molten field's metal bead using a micro manipulator under an optical microscope. The speed of pulling as well as the temperature is precisely controlled to yield good metal spike. As the melting point of Field's metal is 62°C, the temperature of the hotplate was raised to just about 3-5°C higher. This is done to ensure the air just above hotplate quickly cooled to surrounding in order to freeze the pulled field's metal.

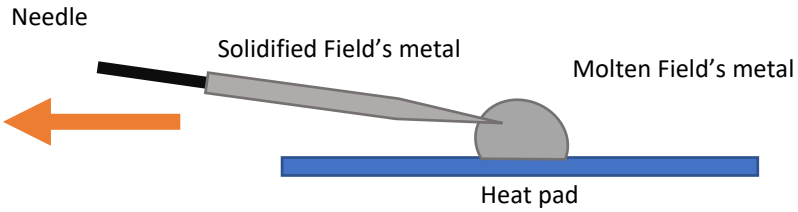

Figure 15: Preparation of Field's metal spike. End of needle is inserted into molten Field's metal bead and carefully pulled out to form long and sharp tip.

After good spike was obtained, the sharp end was precisely positioned to the edge of graphite flake. Then, once again temperature of the hotplate raised above the melting temperature of Field's metal but at slightly higher value approximately at 72°C, so that as the spike touches the sample surface, it melts again forming a continuous wire of metal. Next, the substrate containing the spike was cooled to room temperature, followed by applying conductive paint on the other end of the spike all the way to the STM sample holder.

While this procedure is fast and reproducible, the melted spike on the substrate was found to detach at low temperature in the STM which in my case at 9 K. As a result, the graphite flake is electrically disconnected from the STM sample holder. However, this contacting method is recommended to be used for measurement done at room temperature. The sample which will be discussed in this thesis was prepared using this method with the STM measurement was done at temperature of 300 K (See Figure 16b).

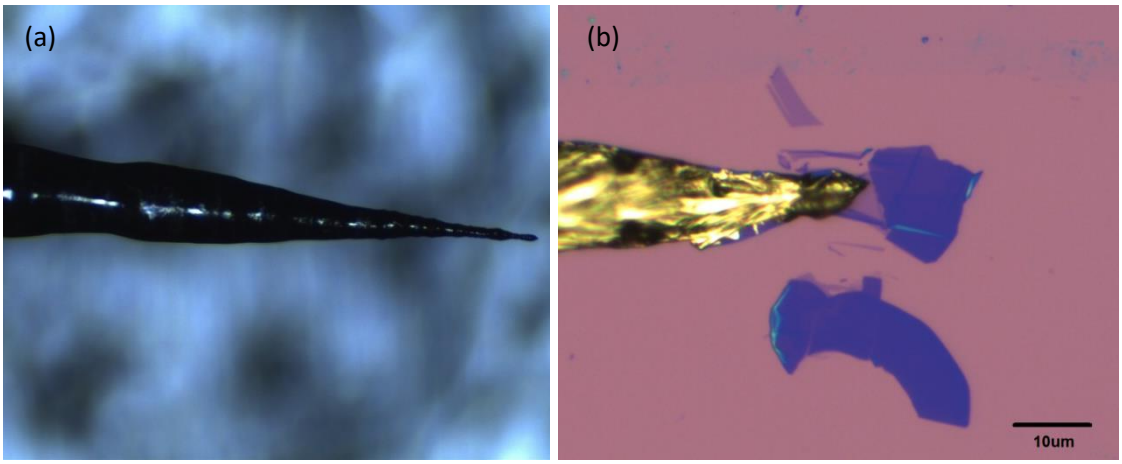

Figure 16: Image shows (a) Long and sharp Field's metal spike and (b) melted spike on top of graphite flake.

Thermal Evaporation of Gold

In this method, I masked the graphite flake using TEM grid that acts as a shadow/stencil mask during a later metal deposition. The choice of TEM grid depends on the size of the sample and its position on the substrate. My sample which is shown in Figure 17a is relatively small, about the size of rectangle 50 x 25 µm, therefore a thin TEM grid bar with a big hole is preferred. I used Copper Grids 2120c manufactured by SPI Supplies with a bar width of 12 µm and a hole width of 113 µm. To further enlarge the grid hole where the metal will be deposited, the bars nearby were cut using sharp metal tweezer.

Next, the TEM grid was placed on a PDMS stamp which had been attached to a microscope glass slide. For better viewing of the grid from the other side of the glass slide, a hole was cut at the center of the PDMS stamp before placing the grid. Next, flux was applied on the edges of the grid to temporarily hold the Field's metal powder. The glass slide was then placed in the transfer system upside down where the PDMS stamp with the TEM grid facing the sample. In

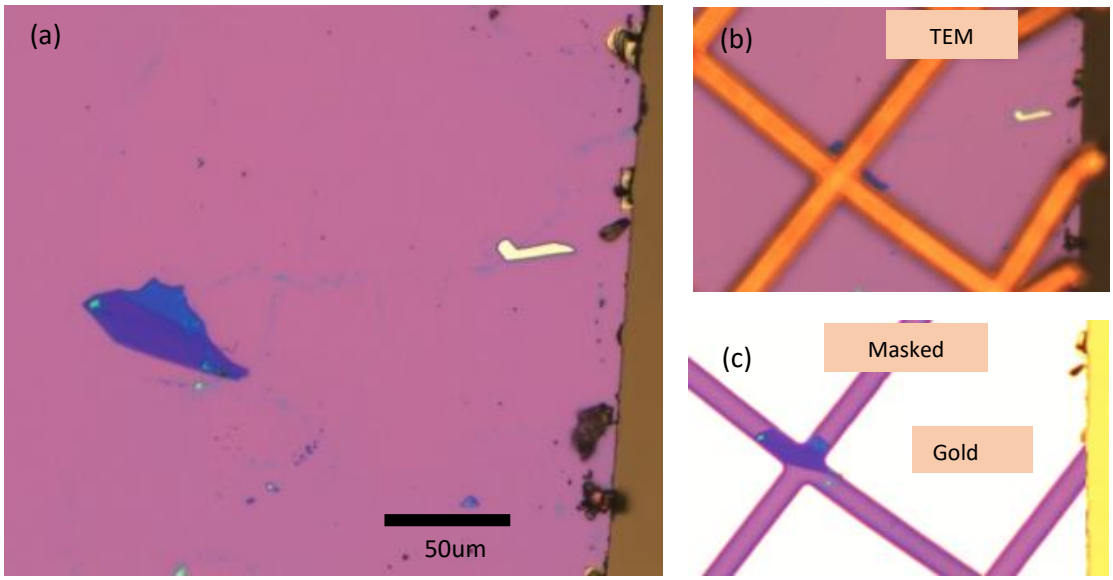

Figure 17: (a) Optical image of graphite flake before masking, (b) after TEM grid placed on top of the flake leaving small area exposed and (c) after gold particles deposited on the substrate

the transfer system, micromanipulator screws were used to accurately position the TEM grid to the graphite flake on the substrate. The temperature of the hot plate which hold the substrate was raised to 72°C to melt the Field's metal powder and thus welding TEM grid to the substrate. After the temperature decreased below 50°C, the glass slide was raised slowly and the TEM grid started to detach from PDMS stamp.

Thermal evaporation technique had been tested with various materials and parameters to ensure the contact of gold is continuous while minimizing the effect to the graphite flake. One of the issues observed is particles diffusing on the graphite surface under the masked area as depicted in Figure 18c.

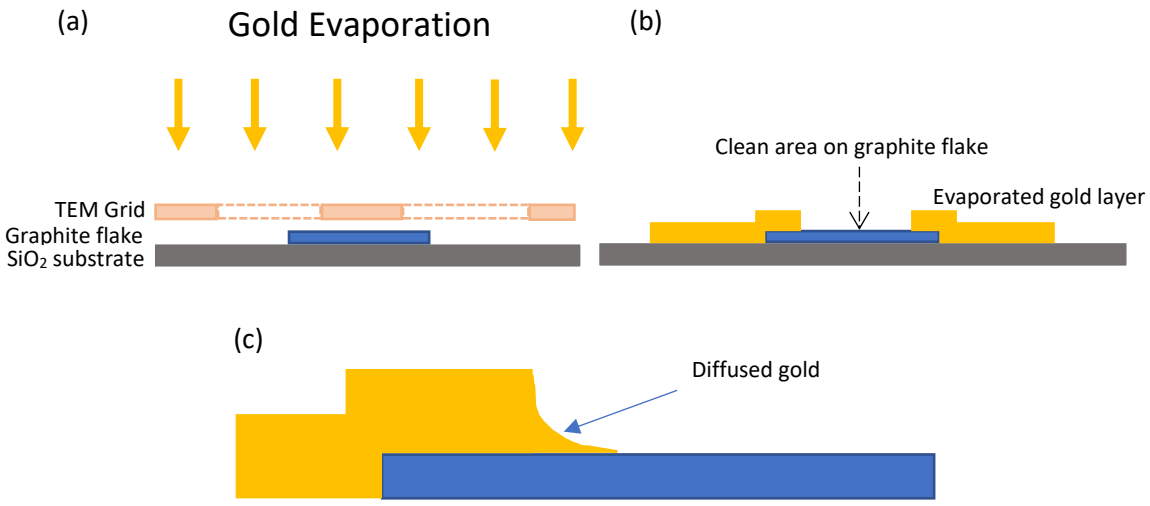

Figure 18: (a) Schematic diagram showing thermal evaporation of gold on graphite flake with TEM grid act as mask. (b) After gold evaporation, clean area on the graphite flake is obtained. (c) Gold particles diffused to the masked area.

I conducted simple experiments to study the effect of the rate of evaporation with different materials. To observe the result of each set, I used tapping mode in Atomic Force Microscopy (AFM) on the masked area of the graphite surface. Figure 19a-c shows the effect of material evaporated to the surface where in (a) gold for 30 nm thickness, (b) titanium 5 nm followed by gold 30 nm and (c) titanium 30 nm. Figure 19a shows long and thin particles in the direction of flowing to bigger particles which indicates high mobility gold particles accumulating. In Figure 19b on the other hand, as titanium is evaporated prior to gold, we can observe significantly smaller mobility with only small traces of gold particle under the stencil. This is because titanium attached better to the substrate and prevents gold particles from being diffused into the masked area. We also tested titanium as the only material to be evaporated as shown in figure 19c. Here we observe very clean surface with no particles except those diffused within the boundary. This shows exceptional adhesion properties of titanium particles which make it good to be the base layer for the deposition. Titanium was not made as main material for metal evaporation due to their oxidative nature. This could affect electrical contact if the titanium starts to oxidize in air. For preventative measures, it is advised the sample evaporated with this method to be kept in an inert environment.

I have also experimented with the rate of evaporation of metal to the substrate. With same materials and thickness, figure 19b shows sample evaporated at 3Å/s whereas sample in figure 19d was evaporated at slower rate which is 0.5Å/s. The difference in the size and dispersion of the particles demonstrates that faster rate gives cleaner surface. At a faster rate, the building of layers is much faster leaving the gold particles less time to diffuse into the masked area.

I made further cleaning of the surface from the small traces of gold particles using contact mode of AFM at relatively small force. In order to minimize interacting with the surface of graphite to avoid any possibility of stacking order change of the layers underneath. In my experiment, the sample was cleaned using a cantilever with force constant of 1.2 N/m, deflection setpoint at -2 V and engaging the surface at 0 V. Next, I contacted the end of the gold pad which touches the graphite flake with carbon conductive paint to connect them with the STM sample holder.

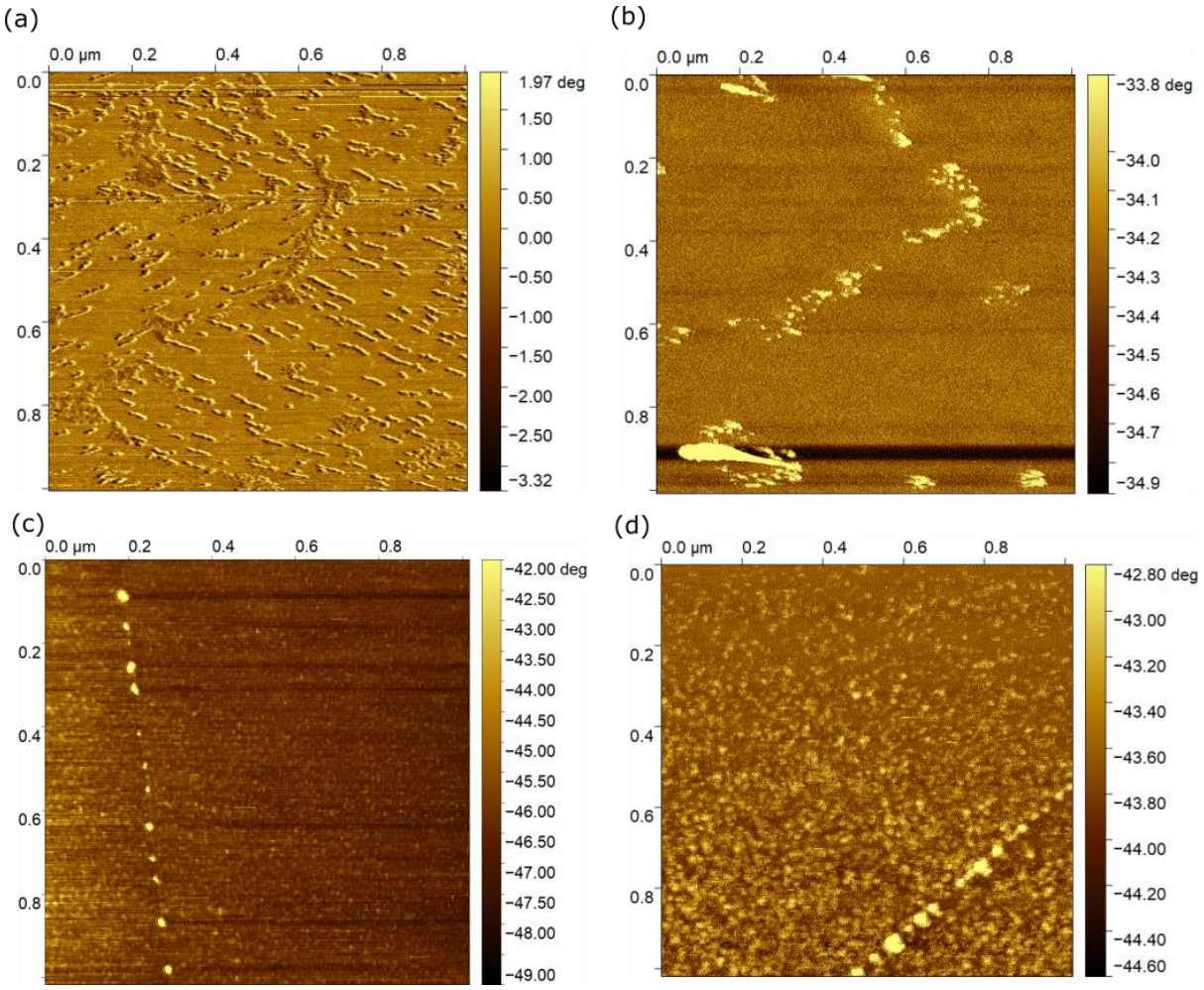

Figure 19: AFM phase image showing surface of graphene undergone thermal evaporation experiment with different parameters. In (a) gold is evaporated for 30 nm at 3Å/s, (b) titanium evaporated for 5 nm followed by gold for 30 nm at rate 3Å/s, (c) titanium evaporated for 30 nm at 3Å/s and (d) titanium evaporated for 5 nm followed by gold for 30 at 0.5Å/s.

2.2 Characterization Technique

2.2.1 Raman Spectroscopy

To identify ABC stacked graphite, the differing vibrational properties of carbon atoms in the ABA and ABC stackings are exploited to determine which stacking order the graphene layers built of by using Raman spectroscopy [35]. This technique has been widely used due to its ability to provide information on lattice disorder, edge and grain boundaries, thickness, and strain of the material [36]. For decades, Raman spectroscopy has been used in the characterization of carbon samples either three-dimensional allotropes such as diamond and graphite, two-dimensional such as graphene or even zero-dimensional such as fullerenes.

The basis of Raman spectroscopy is the interaction of light with the material in the form of inelastic scattering which is called Raman scattering. This is opposite to elastic scattering (Rayleigh scattering) which can be observed at significantly higher intensity. Elastic scattering happens when incident photons excite electrons to a higher level and fall back to same level, thus producing photons with the same energy. If the excited electrons fall to different level from its original state, different energy of photons will be produced. Two possible scattering processes can be measured which are called Stokes transitions: when the photon loses energy due to electron falling to a level higher than the original states; and anti-Stokes transition: when the incident photon gains energy from the system related to vibrational mode of electronic states as shown in Figure 20. We observe Stokes scattering with less probability because the system is less likely to be vibrationally excited prior to irradiation.

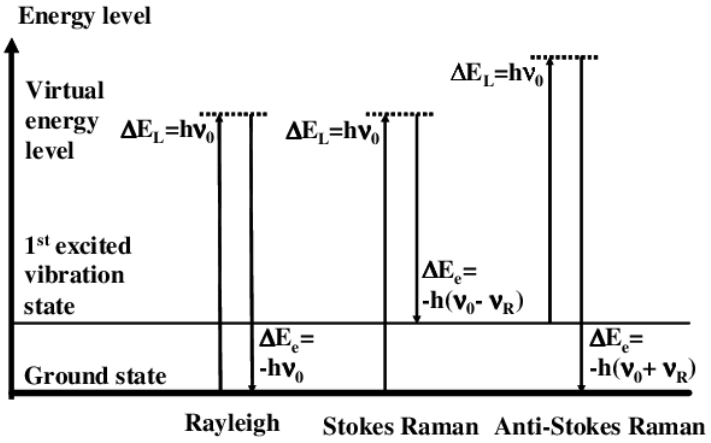

Figure 20: Schematic diagram showing electrons excitation and relaxation after induced with photons. Different energy level involved affect the energy of photon produced which described as Rayleigh scattering, Stokes and anti-Stokes scattering. Image ref [37].

We can observe several Raman peaks which act as a fingerprint of graphene due to Stokes energy shift of the laser excitation. The two peaks with largest intensity are called the G-band which can be found at 1580 cm^{-1} and 2D-band giving the biggest intensity at 2690 cm^{-1}. At lower intensity, we could see the D-band which approximately lies at 1350cm^{-1}. Figure 21 shows the Raman spectroscopy of different carbon structure demonstrating the peak shape and location for each band [38]. The reason for the narrow and sharp peaks in graphene and wider distribution and less intense peak in graphite for example lies in the structure and positioning of carbon atom in the material. Each band represents different characteristics of the material.

G-band provides information about in-plane vibration of sp^2 carbon atoms which technically means the stretching behavior of C-C bond. The intensity and shape of G-band for both graphene and graphite are nearly similar as they both have a planar structure. On the other hand, the G-band of nanotube have wider distribution and two different peaks overlapped at a small distance. This can be explained by the curvature of graphene layers that making up the cylindrical tube structure.

The D-band represents the defects due to disordered structure of crystal. As graphene has a very symmetric six-atoms rings of sp^2 carbon atom, there are no peak detected unless the measurement is close to the edge of graphene flake or to point defects.

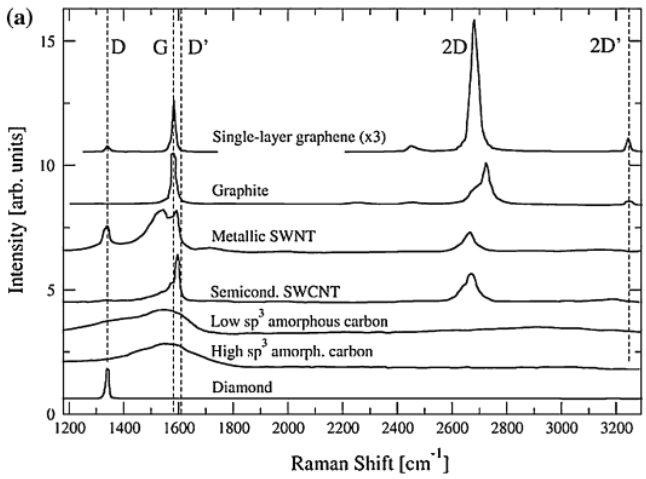

Figure 21: Raman scattering spectra of different Carbon allotropes showing different features due to atomic configuration. Image ref [38].

2D-band indicates the second order effect of D-band and does not require defect or edges to be activated in Raman spectrum. The shape represents the stacking order in the structure. This is the reason why we observe very high and sharp 2D peak in graphene as compared to graphite which is a result of high level of order. Graphite on the other hand has roughly four times lower intensity with broader peak and observable second peak much less level of order due to many layers involved.

Henni et al. [39] studied the stacking effect on 2D peaks comparing ABA and ABC stacking of few layers graphene. Figure 22 shows the 2D peak for ABA stacked (h0) and ABC (h4). Even though both samples have the same number of layers (N=15), the difference can easily be identified where ABC stacked layers have a more intense second peak as indicated by the

arrow. This second peak could be considered a unique fingerprint of ABC graphite [39][40]. By fitting a Lorentzian to the measurements, we can distinguish stacking order easily for which the width of the fitted peak being wider for ABC type graphite.

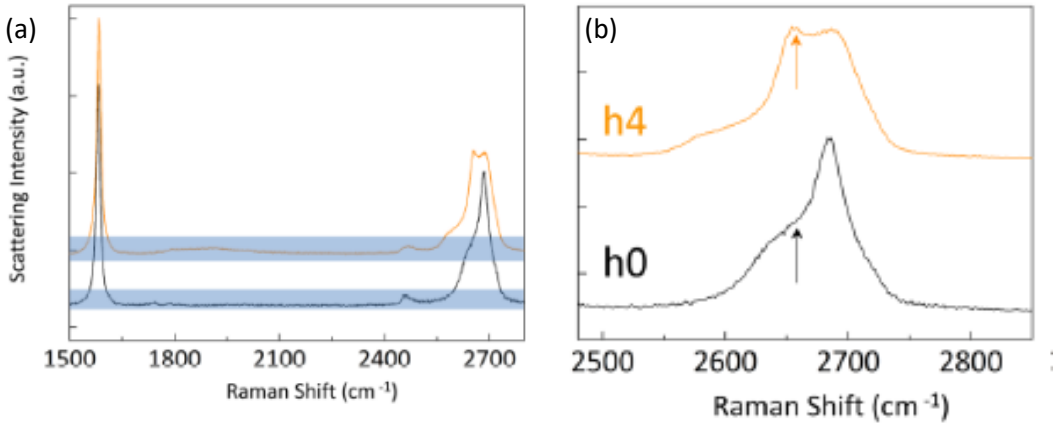

Figure 22: Raman scattering spectra measured on ABC (orange) and ABA (black) stacking region showing two distinct feature in the 2D band. Image ref [41].

2.2.2 Atomic Force Microscopy

The graphene flakes that we obtained can further be analyzed using Atomic Force Microscopy (AFM) to map the topography of the sample surface, characterize the materials on the surface for any foreign molecules/particles and surface cleaning. Samples especially that undergo thermal evaporation will be cleaned in order to ensure the surface is free from dirt.

Conceptually, AFM is a simple technique that employs the interaction between a tip which is attached to a flexible cantilever. The deflection of the cantilever is a measure of the tip-sample force. The forces in atomic level can be divided into two categories: short range/repulsive and long range/attractive (see Figure 23). Long range force includes van der Waals, capillary and electrostatic force while short range force involves chemical bonds or Pauli repulsion forces. Both forces exist approximately between 0.5 nm to 10 nm for long range and less than 0.5 nm for short range [41].

The different effects of these forces can be used to obtain a wide range of information regarding the mechanical properties of the sample surface. Therefore, different techniques can be applied such as contact mode, non-contact mode and tapping mode.

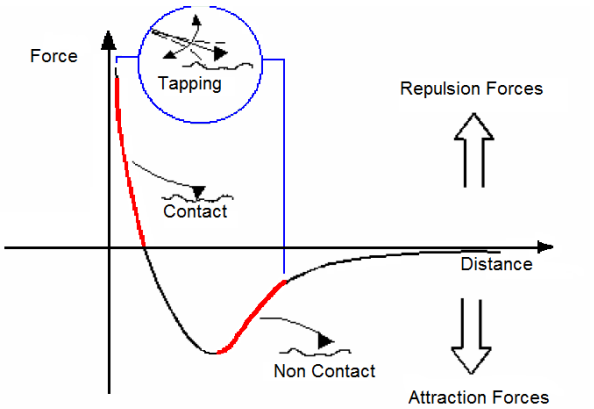

Figure 23: Interaction force versus distance between AFM tip and sample surface. AFM mode works differently relative to distance. Image ref [42].

In my experiment, I used tapping mode for imaging purposes at various scan sizes, ranging from 500 x 500 nm^2 to 50 x 50 μm^2. This helps determine if there are any dirt/particles on the surface which might come from gold evaporation due to diffusion during thermal evaporation or random dirt from air. The search for best area is challenging as my goal was to get a large size of clean surface with at least 15 x 15 μm^2 to allow safe landing of the STM tip onto the flake. Therefore, I apply contact mode where constant force was applied between the tip and sample. The scanning tip was used to drag any surface dirt away as depicted in Figure 24. The cantilever used have the force constant of 1.2 N/m, deflection setpoint at -2 V and engaging the surface at 0 V. After the surface cleaning was finished, the sample was inspected using tapping mode at higher resolution to ensure no more dirt on the surface and to map the surface topography. Finally, the sample was stored in an inert environment to avoid dust or foreign molecule adsorption.

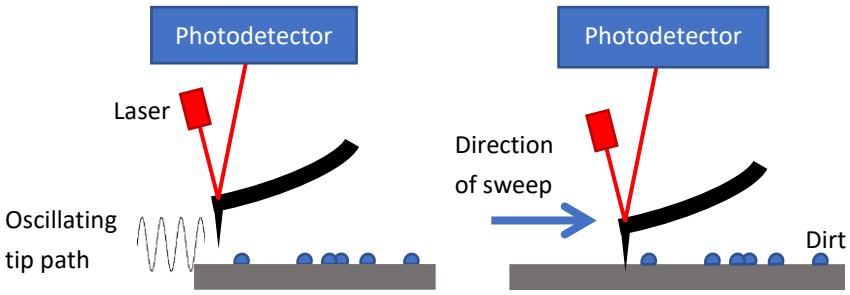

Figure 24: Schematic diagram showing tapping mode where tip oscillating at some predefined frequency in the left and contact mode being used for cleaning the surface.

The topographical map from tapping mode can be used to determine the profile of the sample. We may observe surface defects on the sample, edges of graphene or ripples. On top

of that, we can determine the sample height as shown in Figure 25. From this we can calculate number of graphene layers that make up the sample by dividing height with graphene thickness which is approximately d ≈ 0.335 nm. Our sample as shown below was found to have a height approximately 7 nm. This can be translated as 21 layers of graphene.

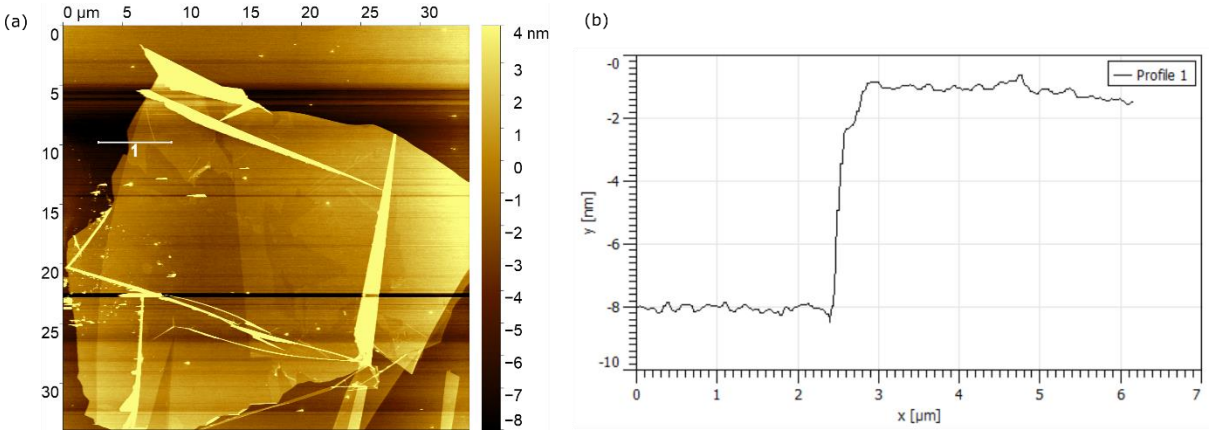

Figure 25: (a) Topographical map of the investigated sample measured using Atomic Force Microscopy. (b) Height profile of line 1 showing height of the flake approximately 7 nm which is equivalent to 21 graphene layers.

2.2.3 Scanning Tunnelling Microscopy

This subchapter will briefly discuss theories and general operation of Scanning Tunneling Microscopy (STM) together with its pair, Scanning Tunneling Spectroscopy (STS). Main part of this research relies on STM/STS for measurement of graphite flakes to investigate its electronic properties especially density of states and band structure. Besides that, a lot of information on the surface structure could be obtained by plotting the topographical map of the sample.

STM works based on the quantum tunneling effect in which probability of electron penetrating a potential barrier larger than its kinetic energy is higher than zero. Main component of STM are tip to form electrical contact with the sample, piezoelectric XY and Z scanner to move tip, feedback system and computer for data collection and analysis.

In STM, the potential barrier is simply vacuum which separates tip from sample under investigation. The height of the barrier is defined as the workfunction, ϕ which is how much energy required by electron to climb up to escape from the Fermi level.

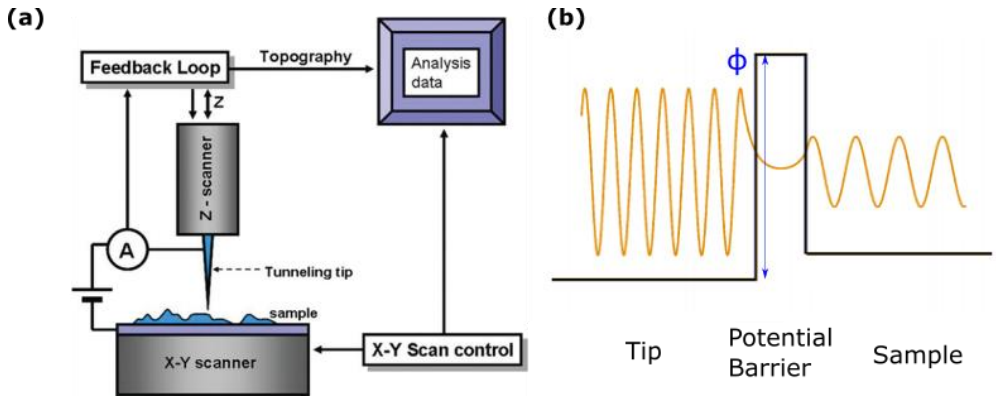

Figure 26: (a) Schematic diagram of Scanning Tunnelling Microscope showing main components and (b) quantum tunnelling of electron passing through potential barrier with height ϕ. Image ref [43].

We can roughly estimate the workfunction of the system as the average of the of sample and tip workfunctions [44]. Each material has different value of workfunction as it depends on the atomic configuration at the surface of the material.

$$\boldsymbol{\Phi} = \frac{1}{2}(\boldsymbol{\Phi}_{sample} + \boldsymbol{\Phi}_{tip})$$

To introduce the working principle of STM, we consider the elementary model of the tunneling process for the one-dimensional case. The solution of Schrödinger equation for an electron in the potential barrier can be written with wavefunction $\Psi(z)$ as:

$$\Psi(z) = \Psi(0)e^{-\boldsymbol{\kappa} z}$$

where $\Psi(0)$ is the wavefunction at z = 0, $\boldsymbol{\kappa} = \frac{\sqrt{2m(\boldsymbol{\Phi}-\mathbf{E})}}{\hbar}$ is decay constant, m is mass of electron, $\hbar$ is Planck's constant, $\boldsymbol{\phi}$ is potential barrier height and **E** is energy of electron. Probability of observing electron at the end of potential barrier is:

$$|\Psi(z)|^2 = |\Psi(0)|^2 e^{-2\boldsymbol{\kappa} z}$$

By applying a small bias voltage V_b, the electrons tunnel to complete the circuit with polarity depending on which side V_b applied to. If the energy of electron is significantly smaller than the workfunction, **E** << $\boldsymbol{\phi}$, the decay constant could be simplified to $\boldsymbol{\kappa} = \frac{\sqrt{2m\boldsymbol{\Phi}}}{\hbar}$. Assuming the tunneling of electron flow is one-dimensional, we could observe the tunneling current, I is

exponentially decaying with the barrier thickness, *z*. This is advantageous for STM as the system is highly sensitive to distance change.

$$I \propto = |\Psi(0)|^2 e^{-2\kappa z}$$

Now we consider Bardeen's description of tunneling which uses time-dependent perturbation theory to get better insight into the physical nature of tunneling [45][46]. Both tip and sample are treated independently by first assuming both bodies are far apart. Schrödinger equations for both systems are:

$$(\mathbf{T} + \mathbf{U}_s)\boldsymbol{\psi}_\mathbf{s} = \mathbf{E}_\mathbf{s}\boldsymbol{\psi}_\mathbf{s}$$
$$(\mathbf{T} + \mathbf{U}_\mathbf{t})\boldsymbol{\psi}_\mathbf{t} = \boldsymbol{\epsilon}_\mathbf{t}\boldsymbol{\psi}_\mathbf{t}$$

where **T** represents operator of the kinetic energy of the electron, $\mathbf{U_S}$ and $\mathbf{U_T}$ is potential, $\boldsymbol{\Psi}_\mathbf{S}$ and $\boldsymbol{\Psi}_\mathbf{T}$ is time-dependent wavefunction to describe the electron, and $\mathbf{E_S}$ and $\mathbf{E_T}$ is kinetic energy of electron for both sample and tip, respectively.

The amplitude of tunneling represented by the tunneling matrix element *M(z)* can be determined by calculating overlapping of both wavefunction from a state ψ of the sample to the state χ of the tip as they get closer. Bardeen introduced separation surface denoted by *S* to replace *z*, which separates tip and sample in which the tip potential is assumed to be zero in the sample and similarly sample potential is zero in the tip region.

$$\mathrm{M}(z) = \frac{\hbar}{2m}\int_{z=z_0}\left(\chi^*\frac{d\psi}{dz} - \psi\frac{d\chi^*}{dz}\right)dS$$

If we keep barrier thickness constant, we can measure tunneling current as sum of the density of states for energy window eV_b by varying bias voltage, V_b where *e* is charge of electron.

$$I = \frac{4\pi e}{\hbar}\int_0^{eV_b} |M(z)|^2 \ [\mathbf{f}(\mathbf{E}) - \mathbf{f}(\mathbf{E} - eV_b)]\ \rho_s(\mathbf{E})\ \rho_t(\mathbf{E} - eV_b)\ \ d\mathbf{E}$$

where **f**(**E**) is Fermi function and ρ_s and ρ_t are density of states of sample and tip, respectively. In STM, the tip is made from metal which in our case is a platinum-iridium (80:20) alloy. Therefore, ρ_t is just some fixed number in the proximity of Fermi level. Matrix element *M(z)* is

also independent of electron energy. Hence, we could further simplify tunneling current equation to:

$$I = \frac{4\pi e}{\hbar}|M(z)|^2\rho_t \int_0^{eV_b} [\mathbf{f}(\mathbf{E}) - \mathbf{f}(\mathbf{E} - eV_b)]\, \rho_s(\mathbf{E}) \quad d\mathbf{E}$$

Here, we observe tunneling current is dependent only to two factors: tip-sample separation and density of states of the sample. In STM, the measurement takes place in a point locally. In a way, we actually measure Local Density of States (LDOS). To calculate LDOS, we simply differentiate the above equation with respect to bias voltage. By rearranging, we obtain:

$$\frac{dI}{dV_b} = \frac{4\pi e^2}{\hbar}|M(z)|^2\, \rho_t\, \rho_s(eV_b)$$

In our STM, when bias voltage is applied, the piezoelectric actuator slowly brings the tip closer to the sample and the feedback system accurately adjust the position until current reaches tunneling current that we have set earlier. To measure current-voltage *I(V)* spectrum, feedback system is turned off and bias voltage is swept for a defined range and the current reading is measured. This method is called Scanning Tunneling Spectroscopy (STS). While it is possible to differentiate the *I(V)* curve to yield dI/dV_b directly, the numerical derivative includes noise in the calculation. This noise may come from various sources such as mechanical noise, thermal noise and flicker noise.

To get better insight into true LDOS, we use a lock-in amplifier to eliminate noise and extract signal using a modulation frequency [47]. A wave generator is used to produce small high-frequency sinusoidal signal which then superimposed to bias voltage. This produces a response to tunneling current which will be recorded by the lock-in amplifier and is called the lock-in current. The component in-phase with the sample bias will be amplified and out-of-phase signals will be diminished. The recorded lock-in current can be read as dI/dV_b directly, and thus representing LDOS. The modulation frequency I used for experiment was 1.3 kHz and the modulation amplitude 20 mV, for room temperature measurements.

Another measurement that can be done with the STM is *I(z)* spectroscopy. This method involves testing the tip quality by measuring tunneling current versus tip-sample separation

[48]. The exponential decay function to describe tunneling current is being used in this technique. Good tip will show exponential decay curve whereas bad tip which may hold foreign material at the end or with damaged end will result in imperfect decay curve.

On top of that, STM is also famously used to map the surface of the material especially at the atomic scale. With the correct setup, we are able to see atomic resolution of the material. This helps a lot especially in our case where different stacking need to be measured. While we do not see the stacking underneath top surface directly, we may determine the region by observing the difference in height or arrangement of atom. In some cases, we can see stacking defect such as ripples, wrinkles or crumples of the graphene sheet which contributed from various sources such as thermal vibration, dislocations, or surface tension during sheet formation [49]. Figure 27a shows our topographical measurement of graphite flake surface with creases and surface boundaries spotted. This surface structure is also confirmed with LDOS measurement using lock-in current with bias voltage set at 700 mV. Further investigation which will be discussed in Chapter 3 reveals that each region made from either ABA or ABC stacking.

All experiments in this thesis were performed in ultrahigh vacuum (UHV) chamber with base pressure below 1 x 10^{-8} Torr at room temperature. To reduce thermal effect due to daily temperature change, we keep the room closed and continuously measure the sample for few days. This will leave the sample stabilized and reduce movement due to thermal drift of the tip - sample assembly.

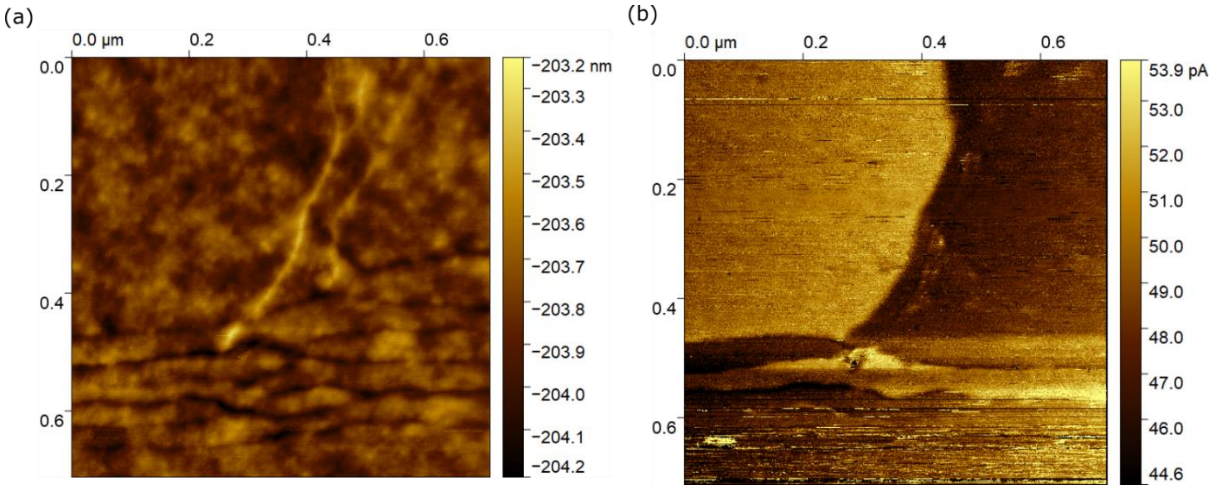

Figure 27: Scanning Tunnelling Microscope measurement on the sample showing (a) topographical map and (b) LDOS map plotted using Gwyddion after measured with V_b = 700 mV, I = 300 pA and lock-in current 50mV.

2.3 Data Processing

Our STM data recorded were processed using Python programming for visualization and data analysis purposes. We obtained LDOS by applying bias voltage V_b in a predefined range and recorded the corresponding lock-in current along the line on the surface. The measured line spectra can be plotted directly with Python. We may observe two distinct shape which indicate the measured point is either ABA or ABC stacked region (see Figure 29c, d). As for ABA region, the LDOS spectra is almost v-shaped with minimum indicating the Dirac point where conduction band and valence band meet. The ABC region on the other hand has a visible peak close to the Dirac point. To distinguish both spectra, we apply 6^{th} degree polynomial to fit the background data with an exception the range where ABC peak is observed. Then, we subtract the background polynomial curve and obtain a peak if the spectra is ABC and no peak if otherwise. The peak is then fitted with a Gaussian function to analyze the features in the form of full width half maximum (FWHM) and peak position in bias voltage. We use FWHM, peak height and peak position in bias voltage to characterize the scanned area for which we could map using these features to observe the interface of the stacking domain.

Chapter 3

Flat Band Properties of ABC Stacked Graphite

In this thesis, the experimental results of thick graphite flakes (N = 21 layers) are presented with the aim of determining the region between ABC and ABA stacked graphene by examining their electronic structure using STM/STS. The stacking regions were identified by Raman spectroscopy mapping to mark our area of interest where we can observe different stacking order in the sample.

As for my sample, Raman scattering intensity at each point on the flake was measured. The 2D peak in the spectra can be categorized as having two different shapes, where the red curve are wider with the peak intensity fluctuating around CCD counts = 1300, whereas the blue curves have two peaks with differing intensity, the smaller intensity is recorded at 2710 cm^{-1} and more intense peak can be found at 2750 cm^{-1} (see figure 28a). This difference in Raman intensity was explained in Chapter 2.2.1 with the red curve associate to ABC stacked graphene and the blue curve to ABA.

The peak can be fitted with a Lorentzian function. The calculated full width half maximum is plotted in a color map as shown in Figure 28b. Alongside the map, I show AFM topographical image of the sample for comparison. The size of the ABC area is quite large, up to almost 50% of the whole sample and located just next to an ABA area. We can clearly distinguish the boundary due to big difference in the width of Lorentzian fit. This advantageous difference allows us to analyze the density of states near the boundary, using STM.

Next, we turn to the STM measurements on the sample. The Lock-In Current from STS spectra recorded along a line is plotted against bias voltage showing two distinct shapes (see Figure 29). As for ABA region, we could see near v-shaped spectra with minimum value close to 0 V. This behavior precisely described the density of states of bulk graphite. However, Dirac point is found to exist at negative voltage bias, V_b = -0.06 V indicating either locally or the whole sample is doped with higher density of electrons. This might arise from Field's metal spike or

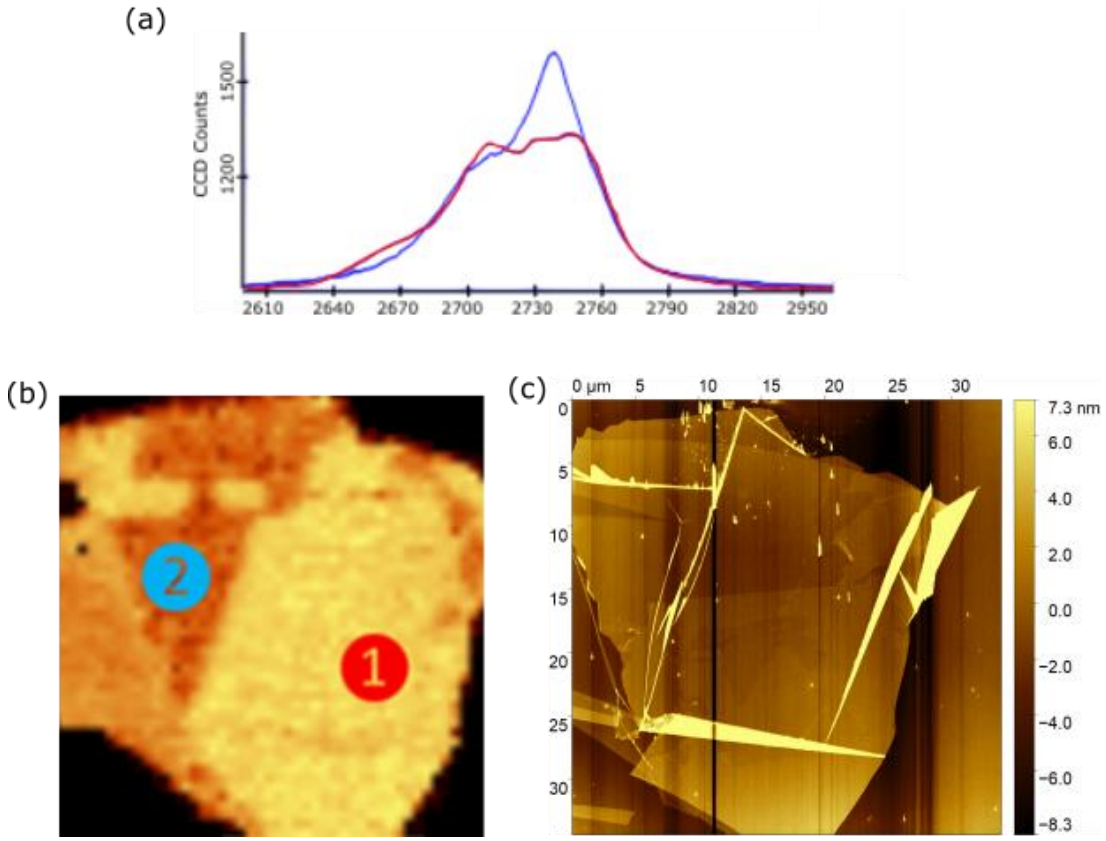

Figure 28: (a) Raman scattering intensities shows different curve shape of 2D band between ABA and ABC region. Each curve is fitted with Lorentzian function to determine FWHM and then mapped as shown in (b). Red curve with bigger FWHM represented by (1) with brighter color indicating ABC stacking underneath whereas blue curve represented by (2) with dark region suggests ABA stacking. In (c), AFM topographical map is shown for comparison.

other impurities on the sample which attached during material preparation. In the ABC region on the other hand, the density of states is found to have peak in the middle at slightly more negative bias voltage than the Fermi level.

Next, LDOS across different regions were measured as shown by the red dotted line where we could observe the evolution of spectra (see Figure 29b). I plot the spectra in a map with the color intensity indicating the height of lock-in current recorded. With ABA and ABC spectra known, we could also observe a mixed region where creases appear within distance approximately 220 nm to 330 nm. This mixed region is identified by observing the sudden change in spectra shape.

To investigate possible inhomogeneities in the local doping, I fit the spectra with 6^{th} degree polynomial and exclude the peak region of ABC approximately between -0.25 V to 0 V. A shift of the Dirac point with respect to the Fermi level (V_b = 0) is a measure of the local doping in the sample. The fitting curve is shown in Figure 29c-d with red dashed line. My measurement

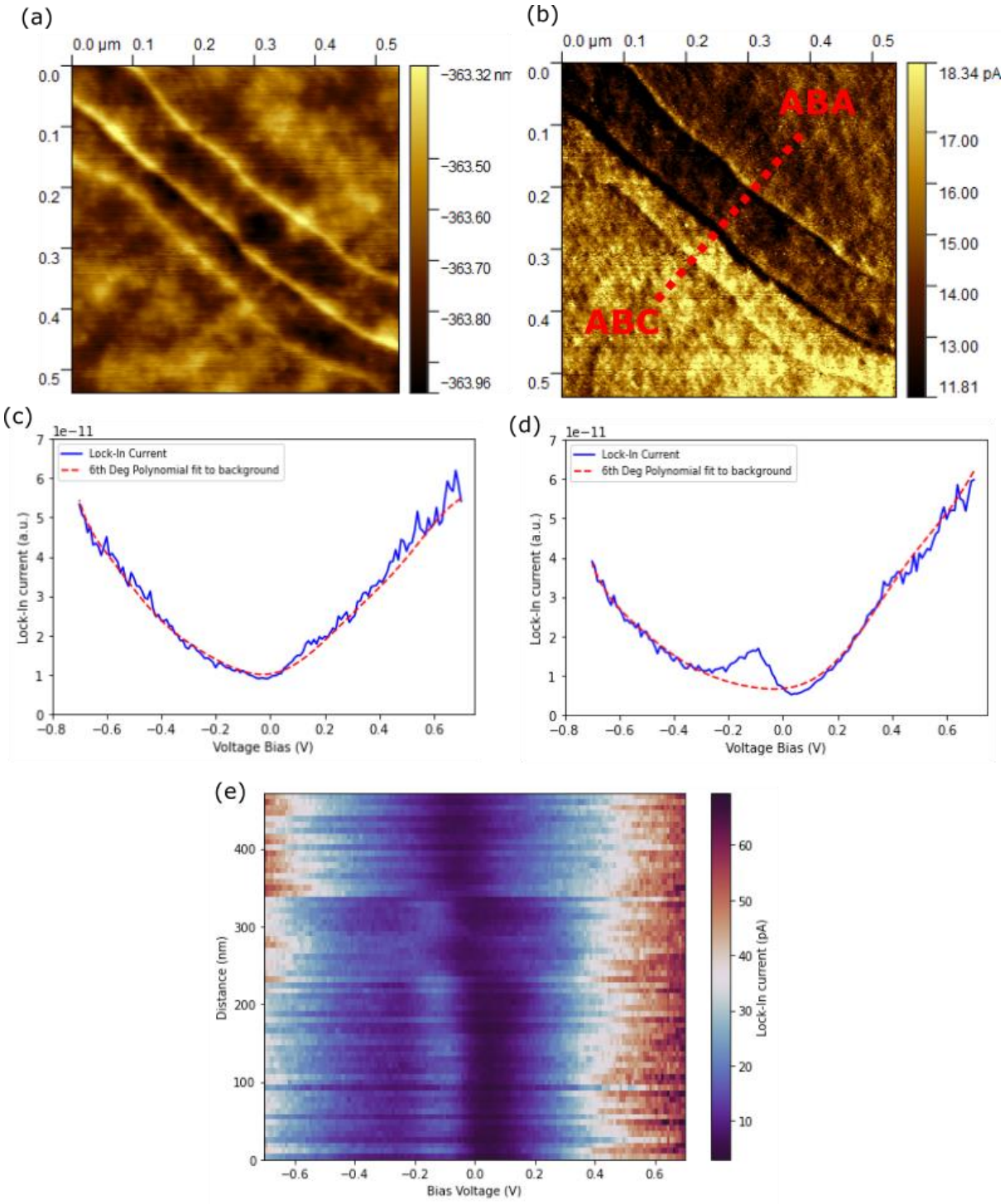

Figure 29: (a) Topographical map of the sample, (b) corresponding LDOS map measured at V_b = -200 mV, I = 500 pA and lock-in current 20 mV showing dark region for ABA stacked graphene and bright region for ABC . (c) LDOS spectra measured using STS on ABA region and (d) ABC. (e) Evolution of LDOS spectra as measured along red dotted line.

in Figure 30 shows the minimum point where Dirac point is considered to exist lies very close to each other within range of -0.07 V to 0 V. Measured points between 45 to 63 where we find the ABA region however, are shifted more to the negative side with the average -0.06 V and standard deviation 0.009 V whereas ABC region were averaged at -0.04 V and distributed

within standard deviation of 0.013 V. Therefore, we could assume the sample is homogeneously doped with minor difference between ABA and ABC. In subchapter 1.4, I discussed that many body interactions create a gap in the flat band. Unfortunately, we could not observe this many body phenomenon since the sample is doped, bringing Dirac point and flat band below the Fermi level.

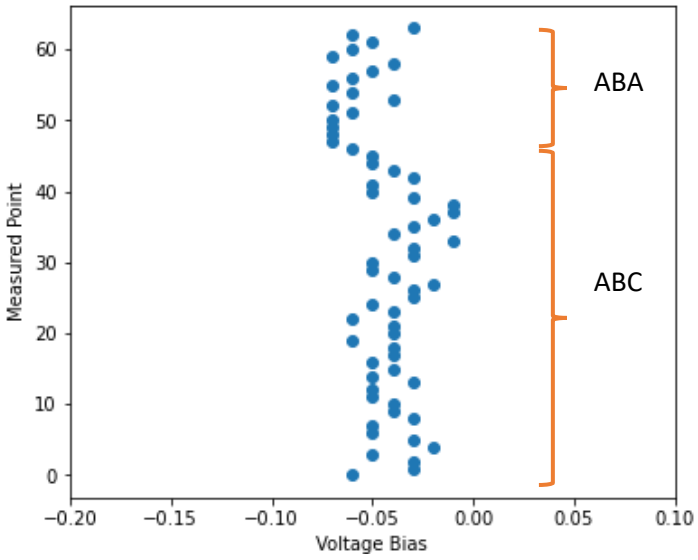

Figure 30: Distribution of minimum for LDOS spectra vs voltage bias.

Next, I fit a Gaussian curve to the flat band peak, such that I can calculate the full width half maximum (FWHM) to see the evolution of spectra by how much FWHM changes along the point in the measured line. My main interest is the mixed area close to the boundary. Figure 31 shows LDOS spectra with different peak sizes. As for smaller peak, the Gaussian width is much bigger. I also calculated the voltage bias where peaks are observed. Along the ABC region, we found that the peak is shifted to -0.135 V from Fermi energy.

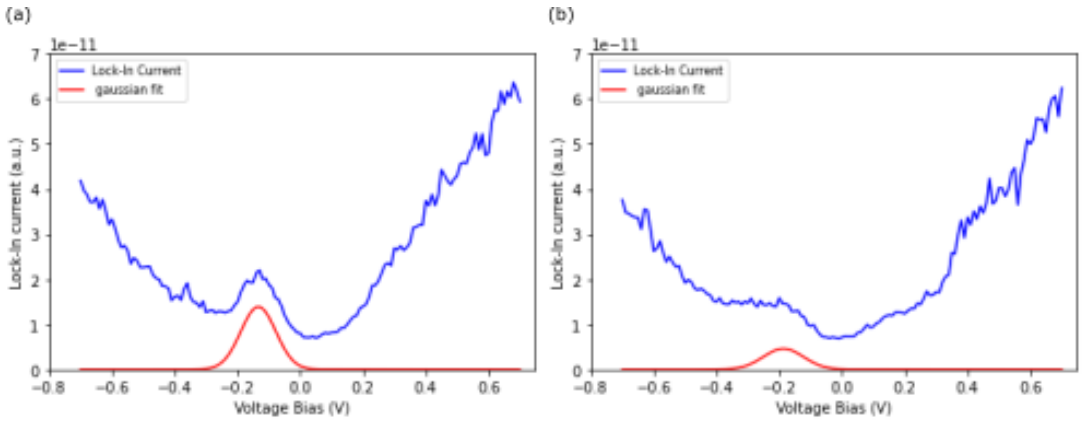

Figure 31: Gaussian curve shown in red after fitting to the peak in LDOS spectra. Different size of peak is observed in different point of measurement.

I then plotted FWHM along the measured line as shown in Figure 32a. The figure denotes that points close to the border have bigger FWHM. Since the width in energy of the flat band decreases as the number of ABC layers increased, we could expect an increase in the FWHM of the LDOS peak, since we expect the ABA – ABC boundary to host a mixture of stackings. Similarly, the Gaussian peak height when plotted shows the decrease in the height from inner region of ABC to the boundary (see Figure 32b). By segregating the region into two groups where the first group containing data for measured point 0 to 32 and the other group holds 32 to 45 points, I calculate the percentage change. Indeed, we observe an increase in the FWHM by 11.7% and decrease in peak height by 37.8%. However, the FWHM and peak height as shown in below figure shows irrational behavior at the very edge of the boundary. This can be explained by the transition of stacking causes wrinkles to the surface which can be found in Figure 29b.

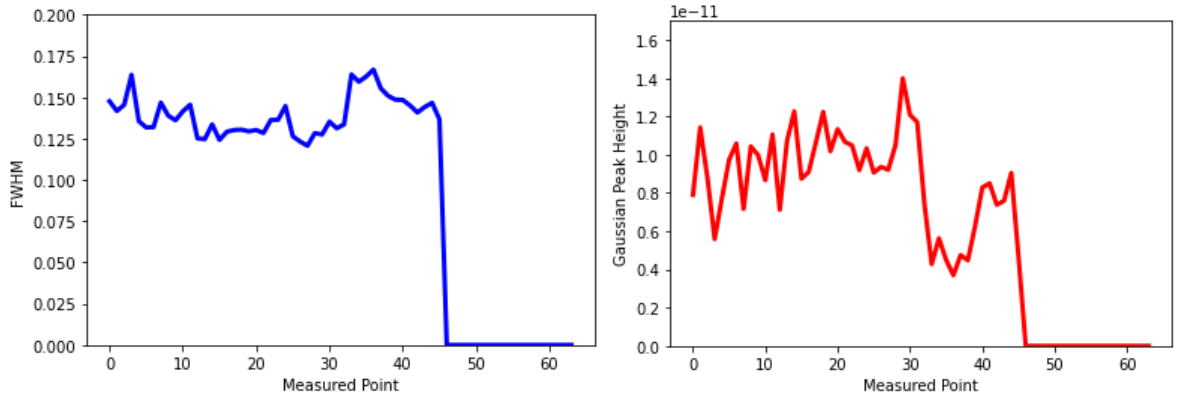

Figure 32: (a) Full width half maximum of calculated Gaussian function from LDOS spectra and (b) Gaussian peak height.

Another measurement on the sample but different area was made. But instead of measuring the spectra across the border, I made two-dimensional measurement of 32 x 32 points to show the area with different stackings more clearly. I show the map of Gaussian peak height which distinguishes peak of pure ABC and mixed stacking more clearly than FWHM. The topographical feature measured with STM is shown together in Figure 33.

In the topographical map, we can observe a quarter circle region in the top left corner and a lot of boundary trenches around this quarter circle. There is another few trench across the area in the lower scanning area that runs horizontally. We can see that the ABC region are separated by wrinkles in the surface from the ABA regions. This is expected since shift in the

local stacking is needed to transform ABC to ABA. It is more energetically favorable for the system to relax this shift by an out of plane buckling of the graphene sheets, leading to a wrinkle.

After all the measured spectra are fitted with a Gaussian function, we can see the map reveals the previously mentioned region. In this calculated map where peak height is plotted as shown in Figure 33b, ABC stacking region where Gaussian peak can be obtained were displayed with brighter color whereas those without peak were set at zero value. However, there are a lot of pixel shown with Gaussian features even though they exist in ABA stacking region. This once again shows how much mixing of different stacking takes place near the border. I show few examples of LDOS spectra obtained on the marked area showing the shape and Gaussian peak features.

The distinction between the LDOS of ABA and ABC stacking in the form of line spectra as previously presented reveals many information in their electronic structure. The main feature of ABC stacking region is the existence of peak close to Dirac point. This peak could be translated as a flat band in the electronic band structure. In Brillouin Zone, this is the region where the number of allowed electron states significantly higher.

The average FWHM of my sample was found to be at 140 meV. This number is actually quite large compared with Henck's where their measurement found that FWHM is just at 50 meV [8]. However, few factors need to be considered to compare both findings side by side. Three main factors that affect the difference are statistical thermal broadening, instrumental setting, and the sample itself. For STM measurements the broadening of LDOS features is given by the empirical formula:

$$\delta E = \sqrt{(3.3k_B T)^2 + (eV_{mod})^2}$$

where k_B is Boltzman constant, T is temperature, e is electron charge and V_{mod} is modulation voltage used in the lock-in amplifier. My measurement was done using STM at room temperature V_{mod} = 20 mV while Henck's sample was measured at 90 K using ARPES. True FWHM for STM measurement was calculated to be 48 meV whereas by only considering thermal broadening in the case of the ARPES measurement, we get 25 meV. The broadened

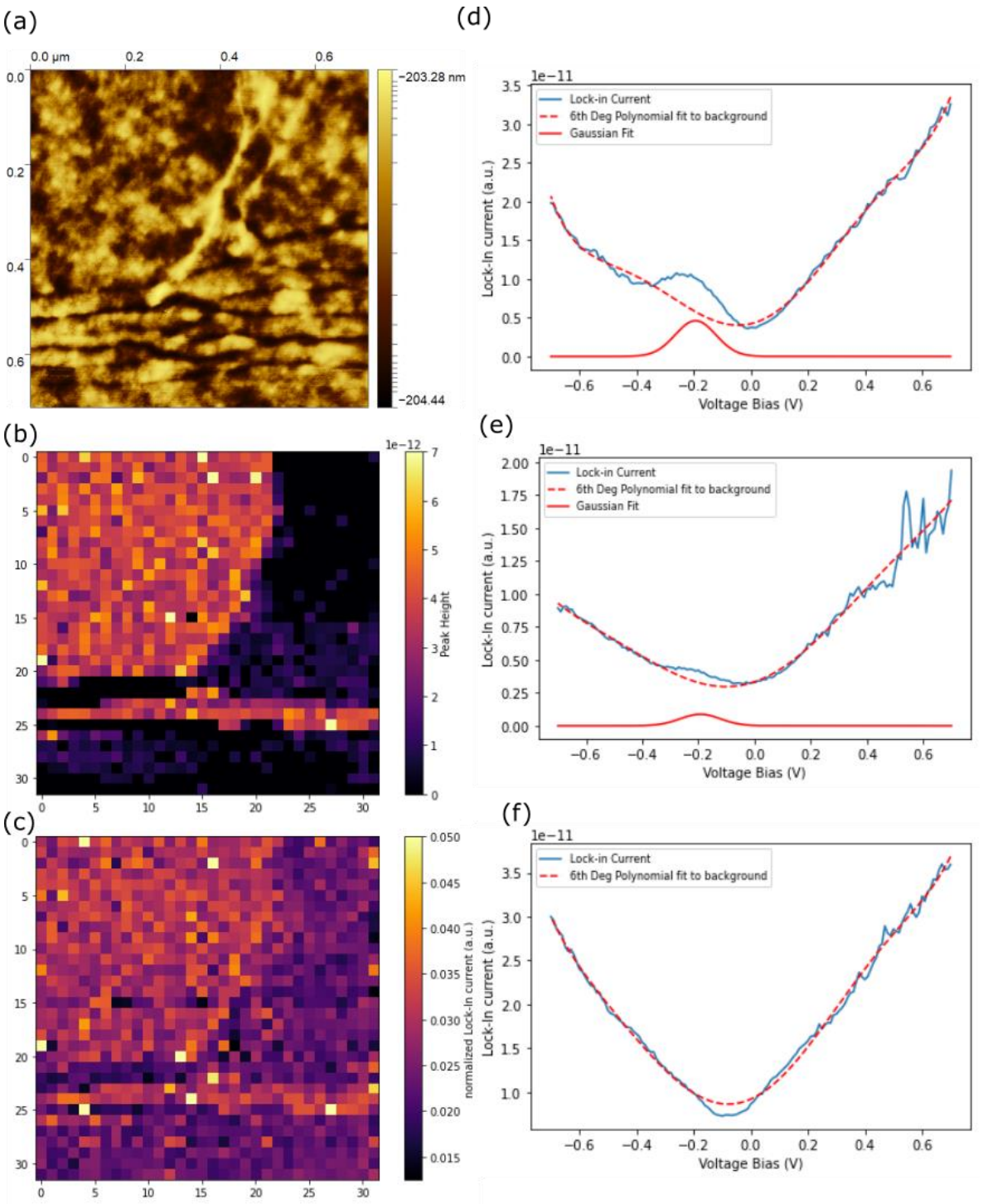

Figure 33: (a) Topolographical map of sample measured using STM and (b) calculated peak height map showing ABC region in bright color and ABA region in black. (c) LDOS image measured at peak voltage where V_b = -200 mV. (d)(e)(f) LDOS spectra for measured point at [2,2], [22,25] and [2,25]

peak both enlarged by high temperature and big V_{mod}. Future work should account for this factor by measuring the sample at low temperature and with small V_{mod} to minimize the broadening effect. The difference between true FWHM between our findings may be intrinsic to the sample.

Chapter 4

Conclusion

In this thesis, I present the STM measurements of the interface between ABC and ABA stacked graphite. My work is the first in the literature to discuss the measurement of ABC properties in bulk graphite. I demonstrate the agreement between Raman spectroscopy and Scanning Tunneling Microscopy to map the stacking order from the sample surface.

As for ABC stacked region, I found the peak in LDOS close to Fermi level with the flat band filled below the Fermi level by 135 meV. This peak represents flat band in electronic band structure of the sample. ABA stacked region on the other hand possesses no visible peak with spectra is v-shaped. The sample doping may stem from adsorbates on the surface, impurities in the graphite itself or, from the Field's metal spike used to contact the sample.

From data analysis, I found that the bandwidth is 140 meV from LDOS spectra fitting. However, after considering broadening of peak, I calculate that true bandwidth is 48 meV. Though this is twice the bandwidth as found by Henck et al. [8], I could consider the difference is intrinsic to the sample and the possible source being stacking disorder, leading to a broader peak then what is expected from the number N = 21 layers.

To continue the research, future work should include the STM measurement at low temperature to reduce the thermal broadening effect and to improve stability of the sample, allowing for atomically resolved spectroscopy measurements. Future work should also include gating of the flat band to the Fermi level in order to investigate many body physics that ABC graphite offered.

Acknowledgement

This thesis is a result of my research work in MTA-EK (Energiatudományi Kutatóközpont) under guidance of Dr. Peter Nemes-Incze. Dr. Nemes-Incze's offer to be a part of his team is highly appreciated. As my principal advisor, Dr. Nemes-Incze has provided me with huge support in my learning and development, especially to be a good experimental physicist. His office was always open if I need help doing experiments or to enlighten my understanding with some physics problems.

Just before I started this MSc work, I made a short study visit to discuss my research interest and possibility of working together in the group. I was warmly welcomed and the people in the institute were happy to accept me to be a part of their team. In my first day in the institute, I met Head of Department of Nanostructures, Dr. Levente Tapasztó to discuss my research experience and how I can contribute to the team. Dr. Levente willingly shared his experience and provided me with a lot of information to work with the team effectively.

I would also like to acknowledge Dr. Gergely Dobrik, Péter Kun and András Pálinkás for their contributions in my research works especially with their advice to conduct experiments successfully. Not to forget my lab partner, Dávid Csikai and Krisztián Márity with their readiness to help each other whenever it is necessary and provided me with good samples for investigation.

Additionally, I would like to thank Dr. Jenő Kürti for his openness to discuss my research problems and become academic advisor of my work.

Last but not least, my parents for always believing in me and encouraging me to follow my dreams. And to my beautiful fiancée, thank you for your continuous support and for being someone who I can talk to whenever I need.

References

1. Landau, L. D. & Lifshitz, E. M. *Statistical Physics, Part I* (Pergamon, Oxford, 1980).

2. Mermin, N. D. Crystalline order in two dimensions. *Phys. Rev.* 176, 250–254 (1968)

3. Geim, A., Novoselov, K. The rise of graphene. Nature Mater 6, 183–191 (2007). https://doi.org/10.1038/nmat1849

4. Novoselov, K. S.; Geim, A. K.; Morozov, S. V.; Jiang, D.; Zhang, Y.; Dubonos, S. V.; Grigorieva, I. V.; Firsov, A. A. (22 October 2004). "Electric Field Effect in Atomically Thin Carbon Films". Science. 306 (5696): 666–669. arXiv:cond-mat/0410550

5. McCann E. (2011) Electronic Properties of Monolayer and Bilayer Graphene. In: Raza H. (eds) Graphene Nanoelectronics. NanoScience and Technology. Springer, Berlin, Heidelberg

6. Zhang, Y. *et al.* Direct observation of a widely tunable bandgap in bilayer graphene. *Nature* 459, 820–3 (2009).].

7. Cao, Y., Fatemi, V., Fang, S. et al. Unconventional superconductivity in magic-angle graphene superlattices. Nature 556, 43–50 (2018). https://doi.org/10.1038/nature26160

8. Henck, H. & Ávila, José & Ben Aziza, Zeineb & Pierucci, Debora & Baima, Jacopo & Pamuk, Betul & Chaste, Julien & Utt, Daniel & Bartos, Miroslav & Nogajewski, Karol & Piot, B. & Orlita, Milan & Potemski, Marek & Calandra, Matteo & Asensio, Maria & Mauri, Francesco & Faugeras, Clément & Ouerghi, Abdelkarim. (2018). Flat electronic bands in long sequences of rhombohedral-stacked graphene. Physical Review B. 97. 10.1103/PhysRevB.97.245421.

9. Min, Hongki & Macdonald, A.. (2008). Electronic Structure of Multilayer Graphene. Progress of Theoretical Physics Supplement - PROG THEOR PHYS SUPPL. 176. 10.1143/PTPS.176.227.

10. Kosynkin, D., Higginbotham, A., Sinitskii, A. et al. Longitudinal unzipping of carbon nanotubes to form graphene nanoribbons. Nature 458, 872–876 (2009). https://doi.org/10.1038/nature07872

11. Li, X., Zhang, G., Bai, X. et al. Highly conducting graphene sheets and Langmuir–Blodgett films. Nature Nanotech 3, 538–542 (2008). https://doi.org/10.1038/nnano.2008.210

12. Reina, Alfonso & Jia, Xiaoting & Ho, John & Nezich, Daniel & Son, Hyungbin & Bulovic, Vladimir & Dresselhaus, Mildred & Kong, Jing. (2009). Large Area, Few-Layer Graphene Films on Arbitrary Substrates by Chemical Vapor Deposition. Nano letters. 9. 30-5. 10.1021/nl801827v.

13. Emtsev, K., Bostwick, A., Horn, K. et al. Towards wafer-size graphene layers by atmospheric pressure graphitization of silicon carbide. Nature Mater 8, 203–207 (2009). https://doi.org/10.1038/nmat2382

14. Chen, G., Sharpe, A.L., Gallagher, P. et al. Signatures of tunable superconductivity in a trilayer graphene moiré superlattice. Nature 572, 215–219 (2019). https://doi.org/10.1038/s41586-019-1393-y

15. Teweldebrhan, Desalegne. (2011). Two-Dimensional Dirac Materials: From Graphene to Topological Insulators.

16. Lee, Changgu & Wei, Xiaoding & Kysar, Jeffrey & Hone, James. (2008). Measurement of the Elastic Properties and Intrinsic Strength of Monolayer Graphene. Science (New York, N.Y.). 321. 385-8. 10.1126/science.1157996.

17. Leggett, J. A., *Lecture 5: Graphene: Electronic band structure and Dirac fermions,* lecture notes, Phys 769: Selected Topics in Condensed Matter Physics, University of California, 2010.

18. Utermohlen, F. (2018) , *Tight-Binding Model for Graphene*.

19. Sarkar, Supratik & Sarkar, Samrat. (2018). Tunneling in Graphene SymFETs.

20. Pike, Nicholas & Stroud, David. (2013). Tight-Binding Model for Adatoms on Graphene: Analytical Density of States, Spectral Function, and Induced Magnetic Moment. Physical Review B. 89. 10.1103/PhysRevB.89.115428.

21. Birowska, Magdalena & Milowska, Karolina & Majewski, J.. (2011). Van Der Waals Density Functionals for Graphene Layers and Graphite. Acta Physica Polonica Series a. 120. 845-848. 10.12693/APhysPolA.120.845.

22. Rozhkov, A. & Sboychakov, A. & Rakhmanov, Alexander & Nori, Franco. (2015). Electronic properties of graphene-based bilayer systems. Physics Reports. 648. 10.1016/j.physrep.2016.07.003.

23. Zhang, W., Yan, J., Chen, C. et al. Molecular adsorption induces the transformation of rhombohedral- to Bernal-stacking order in trilayer graphene. Nat Commun 4, 2074 (2013). https://doi.org/10.1038/ncomms3074

24. Tabert, Calvin & Nicol, Elisabeth. (2012). Dynamical conductivity of AA-stacked bilayer graphene. Phys. Rev. B. 86. 10.1103/PhysRevB.86.075439.

25. Que, Yande & Xiao, Wende & Chen, Hui & Wang, Dongfei & Du, Shixuan & Gao, Hong-Jun. (2015). Stacking-dependent electronic property of trilayer graphene epitaxially grown on Ru(0001). Applied Physics Letters. 107. 10.1063/1.4938466.

26. Pamuk, B., Baima, J., Mauri, F., & Calandra, M. (2017). Magnetic gap opening in rhombohedral-stacked multilayer graphene from first principles. Physical Review B, 95(7). doi:10.1103/physrevb.95.075422.

27. Codecido, Emilio & Wang, Qiyue & Koester, Ryan & Che, Shi & Tian, Haidong & Lv, Rui & Tran, Son & Watanabe, Kenji & Taniguchi, Takashi & Zhang, Fan & Bockrath, Marc & Lau, Jeanie. (2019). Correlated insulating and superconducting states in twisted bilayer graphene below the magic angle. Science Advances. 5. eaaw9770. 10.1126/sciadv.aaw9770.

28. Bistritzer, Rafi & Macdonald, A.. (2010). Moire bands in twisted double-layer graphene. Proceedings of the National Academy of Sciences of the United States of America. 108. 10.1073/pnas.1108174108.

29. Haddadi, Fatemeh & Wu, Quan-Sheng & Kruchkov, Alexander & Yazyev, Oleg. (2020). Moiré Flat Bands in Twisted Double Bilayer Graphene. Nano Letters. XXXX. 10.1021/acs.nanolett.9b05117.

30. Cao, Y., 2016. Electronic Transport In Low-Angle Twisted Bilayer Graphene. Master of Science. Massachusetts Institute of Technology.

31. Nery, Jean & Calandra, Matteo & Mauri, Francesco. (2020). Long-range rhombohedral-stacked graphene through shear.

32. Li, Hongyuan & Utama, M. & Wang, Sheng & Zhao, Wenyu & Zhao, Sihan & Xiao, Xiao & Jiang, Yue & Jiang, Lili & Taniguchi, Takashi & Watanabe, Kenji & Weber-Bargioni, Alexander & Zettl, Alex & Wang, Feng. (2020). Global Control of Stacking-Order Phase Transition by Doping and Electric Field in Few-Layer Graphene. Nano Letters. 20. 10.1021/acs.nanolett.9b05092.

33. Liew, K.M. & Yan, Jian-Wei & Zhang, Lu-Wen. (2017). 2-D Graphene and White Graphene. 10.1016/B978-0-323-43137-8.00009-3.

34. Girit, C. Ö. & Zettl, A. Soldering to a single atomic layer. Appl. Phys. Lett. 91, 193512 (2007)

35. Torche, A., Mauri, F., Charlier, J.-C. & Calandra, M. First-principles determination of the Raman fingerprint of rhombohedral graphite. *Phys. Rev. Mater.* **1,** 041001 (2017)

36. Krishna, Ram & Wade, James & Jones, Abbie & Lasithiotakis, Michael & Mummery, Paul & Marsden, Barry. (2017). An Understanding of Lattice Strain, Defects and Disorder in Nuclear Graphite. Carbon. 124. 10.1016/j.carbon.2017.08.070.

37. Shih, Wei-Chuan & Bechtel, Kate & Feld, Michael. (2020). Non-invasive Glucose Sensing with Raman Spectroscopy.

38. Ferralis, Nicola. (2010). Probing Mechanical Properties of Graphene with Raman Spectroscopy. Journal of Materials Science. 45. 10.1007/s10853-010-4673-3.

39. Henni, Younes & Ojeda Collado, Hector & Nogajewski, Karol & Molas, Maciej & Usaj, Gonzalo & Balseiro, Carlos & Orlita, Milan & Potemski, Marek & Faugeras, Clément. (2016). Rhombohedral Multilayer Graphene: A Magneto-Raman Scattering Study. Nano letters. 16. 3710. 10.1021/acs.nanolett.6b01041.

40. Nguyen, T., Lee, J., Yoon, D. et al. Excitation Energy Dependent Raman Signatures of ABA- and ABC-stacked Few-layer Graphene. Sci Rep 4, 4630 (2015). https://doi.org/10.1038/srep04630

41. Leite, Fabio & Bueno, Carolina & Róz, Alessandra & Ziemath, Ervino & Oliveira, Osvaldo. (2012). Theoretical Models for Surface Forces and Adhesion and Their Measurement Using Atomic Force Microscopy. International Journal of Molecular Sciences. 13. 12773-12856. 10.3390/ijms131012773.

42. Manoel, Jose & Tusset, Angelo & Bueno, Átila & Junior, Bento. (2012). On an Overview of Nonlinear and Chaotic Behavior and Their Controls of an Atomic Force Microscopy (AFM) Vibrating Problem. 10.5772/51834.

43. www.parksystems.com. n.d., Scanning Tunneling Microscopy (STM). [online] Available at: https://parksystems.com/park-spm-modes/94-electrical-properties/241-scanning-tunneling-microscopy-stm.

44. Lounis, Samir. (2014). Theory of Scanning Tunneling Microscopy.

45. Wortmann, D. (2000). Interpretation of Scanning Tunneling Microscopy and Spectroscopy of Magnetic Metal Surfaces by Electron Theory.

46. Hofer, Werner & Redinger, J. (2000). Scanning tunneling microscopy of binary alloys: First principles calculation of the current for PtX (100) surfaces. Surface Science. 447. 51-61. 10.1016/S0039-6028(99)01053-5.

47. Hess, C., *Introduction to Scanning Tunneling Spectroscopy of Correlated Materials*, lecture notes, Autumn School on Correlated Electrons, Forschungszentrum Jülich, 2016.

48. Ginger, D., Overney, R., Sarikaya, M. *Background: Scanning Tunneling Microscopy and Spectroscopy*, lecture notes, Nanoscience on the Tip, University of Washington, 2007.

49. Deng, Shikai & Berry, Vikas. (2015). Wrinkled, rippled and crumpled graphene: An overview of formation mechanism, electronic properties, and applications. Materials Today. 19. 10.1016/j.mattod.2015.10.002.